The current issue and full text archive of this journal is available at
www.emeraldinsight.com/1573-6105.htm

Received 22 September 2010
Revised 23 January 2011
Accepted 10 March 2011

Integration of nonlinear mixed hardening models

Mohammad Rezaiee-Pajand
Department of Civil Engineering, Ferdowsi University of Mashhad, Mashhad, Iran

Cyrus Nasirai
Department of Civil Engineering, Islamic Azad University – Mashhad Branch, Mashhad, Iran, and

Mehrzad Sharifian
Department of Civil Engineering, Ferdowsi University of Mashhad, Mashhad, Iran

Abstract

Purpose – The purpose of this paper is to present a new effective integration method for cyclic plasticity models.

Design/methodology/approach – By defining an integrating factor and an augmented stress vector, the system of differential equations of the constitutive model is converted into a nonlinear dynamical system, which could be solved by an exponential map algorithm.

Findings – The numerical tests show the robustness and high efficiency of the proposed integration scheme.

Research limitations/implications – The von-Mises yield criterion in the regime of small deformation is assumed. In addition, the model obeys a general nonlinear kinematic hardening and an exponential isotropic hardening.

Practical implications – Integrating the constitutive equations in order to update the material state is one of the most important steps in a nonlinear finite element analysis. The accuracy of the integration method could directly influence the result of the elastoplastic analyses.

Originality/value – The paper deals with integrating the constitutive equations in a nonlinear finite element analysis. This subject could be interesting for the academy as well as industry. The proposed exponential-based integration method is more efficient than the classical strategies.

Keywords Differential equations, Vectors, Plasticity, Exponential based integration method, Discrete consistent tangent matrix, Cyclic plasticity, Nonlinear mixed hardening, Exponential isotropic hardening

Paper type Research paper

1. Introduction

The real material behavior under severe loading conditions, is usually explained by plasticity models obeying hardening mechanisms. When the load increases monotonically and no unloading occurs, the linear isotropic and kinematic hardening models present a reasonable description of the material behavior. However, many structures are exposed to cyclic loads, such as earthquake excitations or ocean waves. In these cases, only precise nonlinear isotropic and kinematic hardening constitutive models can predict structural responses.

Multidiscipline Modeling in Materials and Structures
Vol. 7 No. 3, 2011
pp. 266-305

1573-6105
DOI 10.1108/1536-540911178252

In the kinematic hardening mechanism, the yield surface is assumed to undergo the translation in the stress space. Therefore, the hardening rule must consider anisotropy and Bauschinger effect exhibited by real materials. The simplest kinematic hardening mechanism was proposed by Prager (1956). According to this rule, the incremental translation of the yield surface occurs in the direction of the plastic strain increment (Chakrabarty, 2006). As this model could not predict ratcheting, numerous efforts in developing hardening rules have been carried out. All the kinematic hardening models are classified into coupled and uncoupled models (Bari and Hassan, 2000). In the coupled models, the calculating of the plastic modulus is coupled with its kinematic hardening mechanism through the yield surface consistency condition. Several coupled models are suggested by Armstrong and Frederick (1966), Chaboche (1986, 1991, 2008), Ohno and Wang (1993), Abdel-Karim and Ohno (2000), Kang (2004), Abdel-Karim (2009) and Rezaiee-Pajand and Sinaie (2009). In another class of models, the plastic modulus might be indirectly influenced by the kinematic hardening rule but its calculation is not coupled to the kinematic hardening rule through the consistency condition. A number of uncoupled models are suggested by Mroz (1967), Dafalias and Popov (1976) and Tseng and Lee (1983).

A simple mathematical formulation for isotropic hardening is obtained by assuming that the yield surface uniformly expands without any change in shape. This isotropic hardening mechanism has a linear behavior, and the yield surface expansion is a function of the accumulated plastic strain. Although this theory is very straightforward, it is unsuitable to express the behavior of the real materials. For isothermal plastic deformation, Chaboche (1986) suggested a nonlinear isotropic hardening in which the yield surface size reaches saturation after several load cycles. Under cyclic conditions, for some polycrystalline materials, e.g. OFHC copper and stainless steels, plastic strain range memorization can be observed. The phenomenon means that after applying a large cyclic strain range, the subsequent material behavior has been hardened. For lower strain ranges, the stabilized cyclic strength is higher than under normal cyclic conditions without a prior hardening at a larger strain range (Chaboche, 2008). This behavior cannot be taken into account by the isotropic hardening model, in which the yield surface size saturates only once into a fixed value. In this subject, many efforts were done such as Ohno (1982), Ohno and Kachi (1986), Zhang *et al.* (2002) and Kang *et al.* (2003).

One of the key parts in the nonlinear analysis for the elastoplastic evolution problems is the integration of constitutive equations. As analytical solutions for these problems are not commonly available, this process is usually performed by approximate methods. This kind of approximation is mostly carried out by the numerical integration, and normally requires numerous computations. Therefore, the accuracy and robustness of the numerical tactic can play a significant role in elastoplastic analyses. Generally, the integration strategies in plasticity are divided into explicit and implicit categories. In the explicit techniques, updated quantities are only obtained based on the known values at the onset of the load step. In other words, there is no need for any iterative process. One of the well-known explicit schemes is the forward Euler approach. On the other hand, in the implicit methods, updated quantities are determined based on the unknown values at the end of the new load step. Therefore, the solution will have an iterative nature. The return map algorithms, such as the numerical strategies proposed by Wilkins (1964), Rice and Tracey (1973) and Ortiz and Popov (1985) belong to this group. In the past several years, the implicit backward Euler integration methods for cyclic plastic or visco-plastic constitutive models are

provided by Kobayashi and Ohno (2002), Kobayashi *et al.* (2003), Kang (2006) and Kan *et al.* (2007). These tactics give converged solutions even with large load steps.

In the recent decade, the integration methods based on exponential maps are introduced, which are developed in an augmented stress space. First, Hong and Liu (1999) presented the augmented stress space by addition of a component of time and represented the plasticity model in the Minkowski space-time. The researchers showed that the von-Mises plasticity model with linear kinematic hardening could be converted into a system of linear differential equations in the augmented stress space. Afterward, the characteristics of the Minkowski space-time in the constitutive model of the perfect elastic-plastic models and also the models with mixed hardening were investigated (Hong and Liu, 2000a, b; Liu, 2003, 2004). Auricchio and Beirão da Veiga (2003) proposed the exponential maps for solving the differential equation system in the augmented stress space and presented a first-order integration algorithm for the constitutive model with a linear mixed hardening mechanism. Subsequently, this technique was extended to a second-order accuracy scheme (Artioli *et al.*, 2006; Rezaiee-Pajand and Nasirai, 2007). Also, Artioli *et al.* (2007) presented an integration procedure based on exponential maps by considering the von-Mises plasticity with a linear isotropic and Armstrong-Frederick kinematic hardening. A numerical integration based on exponential maps for the Drucker-Prager's elastoplastic models was presented by Rezaiee-Pajand and Nasirai (2008). Rezaiee-Pajand *et al.* (2010) proposed an exponential-based scheme in integrating the constitutive equations along with multi-component nonlinear kinematic hardening. Finally, Rezaiee-Pajand *et al.* (2011) derived an accurate solution and two exponential-based integrations for Drucker-Prager plasticity with linear mixed hardening.

In the present study, the von-Mises criterion with combined multi-component nonlinear kinematic and exponential isotropic hardening are studied for its integration algorithm and consistent tangent modulus. Furthermore, the classical forward Euler method and its discrete consistent tangent operator are presented in detail for the sake of the comparison with the results of the proposed technique. In order to confirm the validity, effectiveness, robustness and performance of the exponential-based method, a wide range of numerical examinations is performed in this study.

To simplify the descriptive relations, all second-rank tensors are considered as nine-dimensional vectors by ordering the tensor components in a vector format. Owing to the symmetry of the second-rank tensors, the number of independent components is reduced to 6. The definition of the trace operator and the Euclidean norm must be modified.

2. Basic equations

A von-Mises yield criterion, with nonlinear isotropic and nonlinear kinematic hardening, in the small strain regime may be written as:

$$F = \|\Sigma\| - R \tag{1}$$

where, $\|\cdot\|$ is the Euclidean norm and R denotes the radius of the yield surface in the deviatoric stress space. Furthermore, Σ is the shifted stress and is defined as follows:

$$\Sigma = \mathbf{s} - \boldsymbol{\alpha} \tag{2}$$

In the above equation, $\mathbf{s}$ and $\boldsymbol{\alpha}$ represent the deviatoric part of the stress and the back stress, respectively. The back stress indicates the center of the yield surface, which evolves

with the kinematic hardening rule. It should be noted, assuming plastic incompressibility, the total back stress and its deviatoric part are identical. The deviatoric stress, $\mathbf{s}$, can be determined by splitting the stress vector $\boldsymbol{\sigma}$, in the following form:

$$\boldsymbol{\sigma} = \mathbf{s} + p\mathbf{i} \quad \text{with } p = \frac{1}{3}\text{tr}(\boldsymbol{\sigma}) \tag{3}$$

where, p is the hydrostatic pressure and "tr" is the trace operator. Also, $\mathbf{i}$ denotes the vector corresponding to the second-rank unit tensor. The total strain $\boldsymbol{\varepsilon}$ can be composed of deviatoric part, $\mathbf{e}$, and volumetric part ε_{v}, as:

$$\boldsymbol{\varepsilon} = \mathbf{e} + \frac{1}{3}\varepsilon_{\text{v}}\mathbf{i} \quad \text{with } \varepsilon_{\text{v}} = \text{tr}(\boldsymbol{\varepsilon}) \tag{4}$$

Since the plastic volumetric strain is equal to zero, the volumetric strain is related to the hydrostatic pressure, with the material bulk modulus K, by the following relation:

$$p = K\varepsilon_{\text{v}} \tag{5}$$

Decomposition of the deviatoric strain into elastic and plastic parts yields:

$$\mathbf{e} = \mathbf{e}^{\text{e}} + \mathbf{e}^{\text{p}} \tag{6}$$

The deviatoric stress is related to the elastic deviatoric strain through the below-generalized Hooke's law:

$$\mathbf{s} = 2G\mathbf{e}^{\text{e}} = 2G(\mathbf{e} - \mathbf{e}^{\text{p}}) \tag{7}$$

where, G is the elastic shear modulus. Using the associative flow rule, the rate of the plastic deviatoric strain can be written as:

$$\dot{\mathbf{e}}^{\text{p}} = \dot{\gamma}\mathbf{n} \tag{8}$$

The term $\dot{\gamma}$ is a proportionality factor, and the vector $\mathbf{n}$ is normal to the yield surface at the contact stress point. Thus, the direction of the vector $\dot{\mathbf{e}}^{\text{p}}$ is $\mathbf{n}$ and its magnitude is equal to $\dot{\gamma}$. In the von-Mises criterion, $\mathbf{n}$ may be obtained by the following relation:

$$\mathbf{n} = \frac{\partial F}{\partial \Sigma} = \frac{\Sigma}{\|\Sigma\|} = \frac{\Sigma}{R} \tag{9}$$

In this study, a nonlinear isotropic hardening rule for the plastic deformation is used, which was originally presented by Chaboche (1986) as follows:

$$\dot{R} = \bar{b}(R_0 + R_{\text{s}} - R)\dot{\gamma} \tag{10}$$

Here, R_0 is the initial radius of the yield surface, $\bar{b}$ and R_{s} are the material constants for isotropic hardening. The off-switch for the evolution of the radius of the yield surface is defined by:

$$\dot{\gamma} = 0 \quad \text{or } R \geq R_0 + R_{\text{s}} \tag{11}$$

The second condition in the above equation shows that the radius of the yield surface will be stabilized if it reaches $R_0 + R_{\text{s}}$. Solving the differential equation (10), with the initial conditions $R = R_0$ and $\gamma = 0$, leads to:

$$R = R_0 + R_{\text{s}}[1 - \exp(-\bar{b}\gamma)] \tag{12}$$

The kinematic hardening mechanism defines the translation of the yield surface during a plastic phase. In this work, a decomposed form of the back stress for the nonlinear kinematic hardening is considered. The most important feature of this rule is the ability to simulate ratcheting in the cyclic plasticity constitutive models. This kinematic hardening rule in its general form can be expressed by the following equations:

$$\dot{\boldsymbol{\alpha}} = \sum_{i=1}^{m} \dot{\boldsymbol{\alpha}}_i, \quad \dot{\boldsymbol{\alpha}}_i = H_{\mathrm{kin},i}\dot{\gamma}\mathbf{n} - \dot{\gamma}A_i\boldsymbol{\alpha}_i \tag{13}$$

where, m is the number of components of the deviatoric back stress vector and $H_{\mathrm{kin},i}$'s are material parameters. The scalar functions that express the dynamic recovery of each component of deviatoric back stress are shown by A_i's. Five different relations for A_i function relevant to five well-known nonlinear kinematic hardening models are given below:

(1) Chaboche (1986) model:

$$A_i = H_{\mathrm{nl},i} \tag{14}$$

(2) Chaboche (1986) model-fourth rule with a threshold:

$$\begin{cases} A_i = H_{\mathrm{nl},i} & \text{for } i \le 3 \\ A_i = H_{\mathrm{nl},i}\left\langle 1 - \frac{\bar{a}}{\|\boldsymbol{\alpha}_i\|}\right\rangle & \text{for } i = 4 \end{cases} \tag{15}$$

(3) Ohno and Wang (1993) model-1:

$$A_i = H_{\mathrm{nl},i}\left\langle \mathbf{n}^{\mathrm{T}}\frac{\boldsymbol{\alpha}_i}{\|\boldsymbol{\alpha}_i\|}\right\rangle \mathrm{H}\left\{\boldsymbol{\alpha}_i^{\mathrm{T}}\boldsymbol{\alpha}_i - \frac{3}{2}\left(\frac{H_{\mathrm{kin},i}}{H_{\mathrm{nl},i}}\right)^2\right\} \tag{16}$$

(4) Ohno and Wang (1993) model-2:

$$A_i = H_{\mathrm{nl},i}\left\langle \mathbf{n}^{\mathrm{T}}\frac{\boldsymbol{\alpha}_i}{\|\boldsymbol{\alpha}_i\|}\right\rangle \left[\left(\frac{H_{\mathrm{nl},i}}{H_{\mathrm{kin},i}}\right)\|\boldsymbol{\alpha}_i\|\right]^{q_i} \tag{17}$$

(5) Abdel-Karim and Ohno (2000) model:

$$A_i = H_{\mathrm{nl},i}\boldsymbol{\mu}_i + H_{\mathrm{nl},i}\left\langle \mathbf{n}^{\mathrm{T}}\frac{\boldsymbol{\alpha}_i}{\|\boldsymbol{\alpha}_i\|} - \mu_i\right\rangle \mathrm{H}\left\{\boldsymbol{\alpha}_i^{\mathrm{T}}\boldsymbol{\alpha}_i - \frac{3}{2}\left(\frac{H_{\mathrm{kin},i}}{H_{\mathrm{nl},i}}\right)^2\right\} \tag{18}$$

In equations (12) through (16), $\bar{a}$, q_i's, $H_{\mathrm{nl},i}$'s and μ_i's are all material constants. Also, H is the Heaviside's step function and $< >$ is the MacCauley brackets, i.e. $\langle x\rangle = (x + |x|)/2$. The Kuhn-Tucker loading-unloading conditions are as follows:

$$\dot{\gamma} \ge 0, \quad F \le 0, \quad \dot{\gamma}F = 0 \tag{19}$$

The material behaves plastically if $\dot{\gamma} > 0$ and elastically when $\dot{\gamma} = 0$. Using the consistency condition during the plastic phase, i.e. $\dot{F} = 0$, and employing equations

of the hardening rules and the associative flow rule, the proportionality factor will be achieved by the following equation:

$$\dot{\gamma} = \frac{2G(\mathbf{n}^{\mathrm{T}}\dot{\mathbf{e}})}{2\bar{G} + \bar{b}(R_{\mathrm{s}} + R_0 - R) - \mathbf{n}^{\mathrm{T}}\sum_{i=1}^{m} A_i \boldsymbol{\alpha}_i} \tag{20}$$

where, $\bar{G}$ is defined with the following relation:

$$2\bar{G} = 2G + \sum_{i=1}^{m} H_{\mathrm{kin},i} \tag{21}$$

3. Integration based on forward Euler method

The forward Euler algorithm is a classical explicit numerical scheme for the stress-updating integration. This integration scheme is straightforward and its results are satisfactory. It uses the first derivative of the yield function and does not require iterative calculations to obtain the updated stress. On the other hand, the final stress at the end of each load step should be corrected to lay on the yield surface because the consistency condition is not involved in the procedure automatically. In this section, the stress-updating algorithm, based on forward Euler method for the von-Mises criterion with combined multi-component nonlinear kinematic and exponential isotropic hardening, is developed. In addition, the tangent operator consistent with the stress-updating algorithm is provided.

3.1 Integration algorithm

In order to integrate the elastoplastic constitutive equations, it is assumed that the rate of strain $\dot{\mathbf{e}}$ is kept constant over each time increment. Therefore, a strain increment $\Delta\mathbf{e}$ over the time interval $[t_n, t_{n+1}]$ is considered. At time t_n, the constitutive variables $\{\mathbf{e}_n, \mathbf{e}_n^{\mathrm{p}}, \mathbf{s}_n, \boldsymbol{\alpha}_n\}$ which characterize the material state are known. The integration algorithm must update the material state at time t_{n+1}. Applying a strain increment $\Delta\mathbf{e} = \mathbf{e}_{n+1} - \mathbf{e}_n$, a trial solution at the end of the time step is obtained as follows:

$$\begin{aligned} \mathbf{s}_{n+1}^{\mathrm{TR}} &= \mathbf{s}_n + 2G\Delta\mathbf{e} \\ \boldsymbol{\alpha}_{n+1}^{\mathrm{TR}} &= \boldsymbol{\alpha}_n \\ \mathbf{e}_{n+1}^{\mathrm{p,TR}} &= \mathbf{e}_n^{\mathrm{p}} \\ \gamma_{n+1}^{\mathrm{TR}} &= \gamma_n \end{aligned} \tag{22}$$

In this stage, the trail solution must be verified to be acceptable. This requires the following condition:

$$\|\mathbf{s}_{n+1}^{\mathrm{TR}} - \boldsymbol{\alpha}_{n+1}^{\mathrm{TR}}\| \le R_{n+1}^{\mathrm{TR}} \quad \text{with } R_{n+1}^{\mathrm{TR}} = R_0 + R_{\mathrm{s}}\left[1 - \exp\left(-\bar{b}\gamma_{n+1}^{\mathrm{TR}}\right)\right] \tag{23}$$

If equation (23) was not satisfied, the step should be divided into an elastic part and a plastic one. Consequently, a scalar parameter $\alpha \in [0,1)$ is introduced to define the elastic part $\alpha\Delta t$, and the plastic portion $[(1 - \alpha)\Delta t]$ of the step. The parameter α can be obtained by these equations:

$$\begin{gathered} \|2G\alpha\Delta\mathbf{e}+\mathbf{s}_n-\boldsymbol{\alpha}_n\|^2=R_n^2 \\ D\alpha^2+2C\alpha+M=0 \\ D=\|2G\Delta\mathbf{e}\|^2,\quad C=2G\Delta\mathbf{e}^{\mathrm{T}}(\mathbf{s}_n-\boldsymbol{\alpha}_n),\quad M=\|\mathbf{s}_n-\boldsymbol{\alpha}_n\|^2-R_n^2 \\ \alpha=\frac{\sqrt{C^2-DM}-C}{D} \end{gathered} \tag{24}$$

Utilizing this scalar parameter, the stress at the end of the elastic part of time step, i.e. at the contact point with the yield surface, can be computed as below:

$$\Sigma^{\mathrm{c}}=\mathbf{s}_n-\boldsymbol{\alpha}_n+2G\alpha\Delta\mathbf{e} \tag{25}$$

Using equations (8) and (20), the increment of the deviatoric plastic strain can be written in the following form:

$$\lambda=\dot{\gamma}(1-\alpha)\Delta t=\frac{2G(\mathbf{n}^{\mathrm{c}})^{\mathrm{T}}(1-\alpha)\Delta\mathbf{e}}{2\bar{G}+\bar{b}(R_{\mathrm{s}}+R_0-R_n)-(\mathbf{n}^{\mathrm{c}})^{\mathrm{T}}\sum_{i=1}^{m}A_i^{\mathrm{c}}\boldsymbol{\alpha}_{n,i}} \tag{26}$$

$$\Delta\mathbf{e}^{\mathrm{p}}=\lambda\,\mathbf{n}^{\mathrm{c}} \tag{27}$$

Then, the deviatoric stress, the center of the yield surface and its radius can be updated by the subsequent equations:

$$\begin{aligned} \mathbf{s}'_{n+1}&=2G\left(\mathbf{e}_{n+1}-\mathbf{e}^{\mathrm{p}}_{n+1}\right) \\ \boldsymbol{\alpha}_{n+1,i}&=\boldsymbol{\alpha}_{n,i}+H_{\mathrm{kin},i}\Delta\mathbf{e}^{\mathrm{p}}-\lambda A_i^{\mathrm{c}}\boldsymbol{\alpha}_{n,i} \\ \boldsymbol{\alpha}_{n+1}&=\sum_{i=1}^{m}\boldsymbol{\alpha}_{n+1,i} \\ \Sigma'_{n+1}&=\mathbf{s}'_{n+1}-\boldsymbol{\alpha}_{n+1} \\ R_{n+1}&=R_0+R_{\mathrm{s}}[1-\exp(-\bar{b}\gamma_{n+1})] \end{aligned} \tag{28}$$

where:

$$\gamma_{n+1}=\gamma_n+\lambda \tag{29}$$

It is evident, since the consistency condition is not automatically satisfied in the forward Euler method, the final stress point will not be laid on the yield surface. In fact, the following correction is required for the solution to guarantee the satisfaction of the consistency condition:

$$\begin{aligned} a_{\mathrm{f}}&=\sqrt{\left(\mathbf{n}^{\mathrm{T}}_{n+1}\Sigma'_{n+1}\right)^2-\|\Sigma'_{n+1}\|^2+R^2_{n+1}}-\mathbf{n}^{\mathrm{T}}_{n+1}\Sigma'_{n+1} \\ \Sigma_{n+1}&=\Sigma'_{n+1}+a_{\mathrm{f}}\mathbf{n}_{n+1} \\ \mathbf{s}_{n+1}&=\mathbf{s}'_{n+1}+a_{\mathrm{f}}\mathbf{n}_{n+1} \end{aligned} \tag{30}$$

In these equations, a_{f} is a scalar parameter that enforces the consistency condition by scaling the stress vector.

3.2 Discrete consistent tangent operator

The consistent tangent matrix is required to preserve the quadratic convergence of the Newton's method in structural analyses. In the following, the discrete consistent tangent operator, i.e. $(\partial\boldsymbol{\sigma}/\partial\boldsymbol{\varepsilon})_{n+1}$ will be presented. Taking the derivative of equation (3) with respect to $\boldsymbol{\varepsilon}_{n+1}$, and utilizing equations (2) and (5), lead to:

$$\frac{\partial\boldsymbol{\sigma}_{n+1}}{\partial\boldsymbol{\varepsilon}_{n+1}} = \left(\frac{\partial\Sigma_{n+1}}{\partial\mathbf{e}_{n+1}} + \frac{\partial\boldsymbol{\alpha}_{n+1}}{\partial\mathbf{e}_{n+1}}\right)\mathbb{I}_{\text{dev}} + K(\mathbf{i}\mathbf{i}^{\text{T}}) \tag{31}$$

$$\mathbb{I}_{\text{dev}} = \mathbb{I} - \frac{1}{3}(\mathbf{i}\mathbf{i}^{\text{T}}) \tag{32}$$

The derivatives $(\partial\Sigma_{n+1}/\partial\mathbf{e}_{n+1})$ and $(\partial\boldsymbol{\alpha}_{n+1}/\partial\mathbf{e}_{n+1})$, which are appeared in equation (31) are presented by:

$$\frac{\partial\Sigma_{n+1}}{\partial\mathbf{e}_{n+1}} = \frac{\partial\Sigma'_{n+1}}{\partial\mathbf{e}_{n+1}} + \frac{\partial a_{\text{f}}}{\partial\mathbf{e}_{n+1}}\mathbf{n}^{\text{T}}_{n+1} + a_{\text{f}}\frac{\partial\mathbf{n}_{n+1}}{\partial\mathbf{e}_{n+1}} \tag{33}$$

$$\frac{\partial\boldsymbol{\alpha}_{n+1}}{\partial\mathbf{e}_{n+1}} = \sum_{i=1}^{m}\frac{\partial\boldsymbol{\alpha}_{n+1,i}}{\partial\mathbf{e}_{n+1}} \tag{34}$$

where:

$$\frac{\partial\boldsymbol{\alpha}_{n+1,i}}{\partial\mathbf{e}_{n+1}} = H_{\text{kin},i}\frac{\partial\Delta\mathbf{e}^{\text{p}}}{\partial\mathbf{e}_{n+1}} - \frac{\partial\lambda}{\partial\mathbf{e}_{n+1}}\left(A^{\text{c}}_i\boldsymbol{\alpha}_{n,i}\right)^{\text{T}} - \lambda\boldsymbol{\alpha}_{n,i}\left(\frac{\partial A^{\text{c}}_i}{\partial\mathbf{e}_{n+1}}\right)^{\text{T}} \tag{35}$$

The derivative $(\partial A^{\text{c}}_i/\partial\mathbf{e}_{n+1})$ in the last equation is dependent on the kinematic hardening mechanisms, i.e. equations (14) through (18), and presented in Appendix 1. Furthermore, the other derivatives appeared in equations (33) and (35) are addressed in Appendix 2.

4. A new integration method based on exponential maps

By defining an integrating factor and an augmented stress vector, the system of differential equations of the constitutive model could be converted into the following dynamical system, which can be solved by an exponential map algorithm:

$$\dot{\mathbf{X}} = \mathbb{B}\mathbf{X} \tag{36}$$

In this equation, $\mathbf{X}$ is an augmented stress vector with $n+1$ components, and $\mathbb{B}$ is a matrix that in nonlinear hardening models is depended on the vector $\mathbf{X}$. In this section, the dynamical system for the von-Mises plasticity model, with combined multi-component nonlinear kinematic and exponential isotropic hardening, is developed. Subsequently, a numerical algorithm for solving the system of differential equations is presented. Finally, the tangent operator consistent with the integration algorithm is provided.

4.1 Mapping to augmented stress space

Initially, a system of differential equations for the shifted stress is developed, and then an integrating factor will be introduced. This will lead to a dynamical system in the augmented stress space. Taking the derivative in time from equation (2) and using equations (7), (13) and (21) lead to:

$$\dot{\Sigma} = 2G\dot{\mathbf{e}} + \dot{\gamma}\sum_{i=1}^{m} A_i\boldsymbol{\alpha}_i - 2\bar{G}\dot{\mathbf{e}}^{\mathrm{p}} \tag{37}$$

Substituting equation (8) into above relation and performing some manipulations yield:

$$\dot{\Sigma} + 2\bar{G}\frac{\Sigma}{R}\dot{\gamma} = 2G\dot{\boldsymbol{\Phi}} \tag{38}$$

where, the vector $\dot{\boldsymbol{\Phi}}$ is defined by the following equation:

$$\dot{\boldsymbol{\Phi}} = \dot{\mathbf{e}} + \frac{\dot{\gamma}}{2G}\sum_{i=1}^{m} A_i\boldsymbol{\alpha}_i \tag{39}$$

In this stage, a dimensionless shifted stress is introduced as follows:

$$\bar{\Sigma} = \frac{\Sigma}{R} \tag{40}$$

Note that in the plastic phase, the vector $\bar{\Sigma}$ is equal to $\mathbf{n}$. Taking the derivative in time from the last equation and using equation (12) will give:

$$\dot{\bar{\Sigma}} = \frac{\dot{\Sigma}}{R} - \frac{R_{\mathrm{s}}\bar{b}\ \exp(-\bar{b}\gamma)}{R}\dot{\gamma}\bar{\Sigma} \tag{41}$$

Using equations (40) and (41), the system of nonlinear differential equations, which is presented in equation (38), can be rewritten in the following form:

$$\dot{\bar{\Sigma}} + \left(\frac{2\bar{G} + R_{\mathrm{s}}\bar{b}\ \exp(-\bar{b}\gamma)}{R}\right)\dot{\gamma}\bar{\Sigma} = \frac{2G}{R}\dot{\boldsymbol{\Phi}} \tag{42}$$

This equation is valid for both elastic and plastic phases. To solve equation (42), an integrating factor X^0 is introduced by the following relation:

$$X^0\dot{\bar{\Sigma}} + X^0\left(\frac{2\bar{G} + R_{\mathrm{s}}\bar{b}\ \exp(-\bar{b}\gamma)}{R}\right)\dot{\gamma}\bar{\Sigma} = \frac{\mathrm{d}}{\mathrm{d}t}(X^0\bar{\Sigma}) \tag{43}$$

Equation (43) gives an ordinary differential equation as:

$$\dot{X}^0 = \left(\frac{2\bar{G} + R_{\mathrm{s}}\bar{b}\ \exp(-\bar{b}\gamma)}{R}\right)\dot{\gamma}X^0 \tag{44}$$

Solving the recent equation with the initial value $X^0(0) = 1$, yields the following result:

$$X^0(\gamma) = \begin{cases} \left(\frac{(R_0+R_{\mathrm{s}})\ \exp(\bar{b}\gamma)-R_{\mathrm{s}}}{R_0}\right)^{1/\beta}\exp(-\bar{b}\gamma) & \text{for } \bar{b} \neq 0 \\ \exp\left(\frac{2\bar{G}}{R_0}\ \gamma\right) & \text{for } \bar{b} = 0 \end{cases} \tag{45}$$

$$\beta = \frac{\bar{b}(R_0 + R_{\mathrm{s}})}{2\bar{G} + \bar{b}(R_0 + R_{\mathrm{s}})} \tag{46}$$

Multiplying equation (42) by the integrating factor X^0 and using equation (43) lead to:

$$\frac{\mathrm{d}}{\mathrm{d}t}(X^0\bar{\boldsymbol{\Sigma}}) = X^0\frac{2G}{R}\dot{\boldsymbol{\Phi}} \tag{47}$$

Taking the scalar product of the last equation by the vector $\bar{\boldsymbol{\Sigma}}$, gives the coming next equation:

$$\frac{X^0}{2}\frac{\mathrm{d}}{\mathrm{d}t}\|\bar{\boldsymbol{\Sigma}}\|^2 + \dot{X}^0\|\bar{\boldsymbol{\Sigma}}\|^2 = \frac{2G}{R}\dot{\boldsymbol{\Phi}}^{\mathrm{T}}(X^0\bar{\boldsymbol{\Sigma}}) \tag{48}$$

Noting that in the plastic phase, $\|\bar{\boldsymbol{\Sigma}}\| = \|\mathbf{n}\| = 1$ and inserting this into the last equation, one can easily obtain:

$$\dot{X}^0 = \frac{2G}{R}\dot{\boldsymbol{\Phi}}^{\mathrm{T}}(X^0\bar{\boldsymbol{\Sigma}}) \tag{49}$$

Using equations (47) and (49), a system of differential equations in the augmented stress space will be achieved:

$$\frac{\mathrm{d}}{\mathrm{d}t}\begin{Bmatrix} X^0\bar{\boldsymbol{\Sigma}} \\ X^0 \end{Bmatrix} = \frac{2G}{R}\begin{bmatrix} \mathbb{O}_{9\times9} & \dot{\boldsymbol{\Phi}} \\ \dot{\boldsymbol{\Phi}}^{\mathrm{T}} & 0 \end{bmatrix}\begin{Bmatrix} X^0\bar{\boldsymbol{\Sigma}} \\ X^0 \end{Bmatrix} \tag{50}$$

Now, a vector and a matrix in the $n+1$ dimensional space are defined by:

$$\mathbf{X} = \begin{Bmatrix} X^0\bar{\boldsymbol{\Sigma}} \\ X^0 \end{Bmatrix} = \begin{Bmatrix} \mathbf{X}^{\mathrm{s}} \\ X^0 \end{Bmatrix} \tag{51}$$

$$\mathbb{B} = \frac{2G}{R}\begin{bmatrix} \mathbb{O}_{9\times9} & \dot{\boldsymbol{\Phi}} \\ \dot{\boldsymbol{\Phi}}^{\mathrm{T}} & 0 \end{bmatrix}_{10\times10} \tag{52}$$

where, $\mathbf{X}$ is an augmented stress vector and $\mathbb{O}_{9\times9}$ is a null matrix. Consequently, equation (50) can be written in the form of a dynamical system in the augmented stress space:

$$\dot{\mathbf{X}} = \mathbb{B}\mathbf{X} \tag{53}$$

In the elastic phase, the control matrix $\mathbb{B}$ can be expressed as:

$$\mathbb{B} = \frac{2G}{R}\begin{bmatrix} \mathbb{O}_{9\times9} & \dot{\mathbf{e}} \\ \mathbf{0}^{\mathrm{T}} & 0 \end{bmatrix}_{10\times10} \tag{54}$$

Here, $\mathbf{0}$ is a null vector with nine dimensions. Note that, in the plastic phase, the matrix $\mathbb{B}$ is dependent on the vector $\mathbf{X}$. As a result, the differential equation (53) will be nonlinear.

The ON-OFF switch for the plastic phase in the augmented stress space can be expressed by the next conditions:

- The stress state must be on the yield surface, i.e.:

$$\|\mathbf{X}^{\mathrm{s}}\|^2 = (X^0)^2 \tag{55}$$

- The rate of the deviatoric strain must be outward with respect to the yield surface, i.e.:

$$(\mathbf{X}^{s})^{T}\dot{\mathbf{e}} > 0 \tag{56}$$

Whenever these conditions are satisfied simultaneously, the switch is ON.

4.2 Augmented stress-updating algorithm

Updating stress in the augmented stress space requires to solve the system of differential equation (53). It is clear, the vector $\mathbf{X} = \mathbf{X}(t)$ is a function of time. If $\mathbb{B}$ is assumed independent of time, equation (53) will be a system of linear ordinary differential equations. Considering initial condition $\mathbf{X}(0)$, the solution of this system can be expressed by the following relation:

$$\mathbf{X}(t) = \exp(\mathbb{B}t)\mathbf{X}(0) \tag{57}$$

As the strain-controlled path is assumed to be a rectilinear path, in a fully explicit manner, R and α are constant over each time step. The known values of these parameters at the beginning of each time step, i.e. R_n and $\boldsymbol{\alpha}_n$, are the values considered throughout the time interval. Consequently, the matrix $\mathbb{B}$ will be independent of the vector $\mathbf{X}$, and the augmented stress vector at the time t_{n+1} can be updated as:

$$\mathbf{X}_{n+1} = \exp(\bar{\mathbb{B}}_n)\mathbf{X}_n = \mathbb{G}_n\mathbf{X}_n \tag{58}$$

where, $\bar{\mathbb{B}}_n = \Delta t\mathbb{B}_n$ in the plastic phase can be expressed by:

$$\bar{\mathbb{B}}_n = \begin{bmatrix} \mathbb{O}_{9\times9} & \frac{2G}{R_n}\Delta\boldsymbol{\Phi} \\ \frac{2G}{R_n}\Delta\boldsymbol{\Phi}^{T} & 0 \end{bmatrix} \tag{59}$$

In this equation, $\Delta\boldsymbol{\Phi} = \Delta t\dot{\boldsymbol{\Phi}}$ leads to the below result:

$$\Delta\boldsymbol{\Phi} = \Delta\mathbf{e} + \frac{\mathbf{n}_n^{T}\Delta\mathbf{e}}{2\bar{G} + \bar{b}(R_s + R_0 - R_n) - \mathbf{n}_n^{T}\sum_{i=1}^{m}A_{n,i}\boldsymbol{\alpha}_{n,i}}\sum_{i=1}^{m}A_{n,i}\boldsymbol{\alpha}_{n,i} \tag{60}$$

It should be mentioned that the matrix exponential in the equation (58) can be presented by a matrix power series or in the following compact form:

$$\mathbb{G}^{e} = \begin{bmatrix} \mathbb{I}_{9\times9} & \frac{2G}{R_n}\Delta\mathbf{e} \\ \mathbf{0}^{T} & 1 \end{bmatrix} \quad \text{elastic phase} \tag{61}$$

$$\mathbb{G}^{p} = \begin{bmatrix} \mathbb{I}_{9\times9} + (a-1)\Delta\hat{\boldsymbol{\Phi}}\Delta\hat{\boldsymbol{\Phi}}^{T} & b\Delta\hat{\boldsymbol{\Phi}} \\ b\Delta\hat{\boldsymbol{\Phi}}^{T} & a \end{bmatrix} \quad \text{plastic phase} \tag{62}$$

where, $\Delta\hat{\boldsymbol{\Phi}}$ is the unit vector of $\Delta\boldsymbol{\Phi}$, i.e. $\Delta\hat{\boldsymbol{\Phi}} = (\Delta\boldsymbol{\Phi}/\|\Delta\boldsymbol{\Phi}\|)$. Also, the parameters a and b are defined as:

$$a = \cosh(g), \quad b = \sinh(g), \quad g = \frac{2G}{R_n}\|\Delta\boldsymbol{\Phi}\| \tag{63}$$

As it was mentioned before, the initial value of X^0 is equal to 1. Therefore, the initial value for the augmented stress vector will be as follows:

$$\mathbf{X}(0) = \begin{Bmatrix} \mathbf{X}_0^{\mathrm{s}} \\ 1 \end{Bmatrix} = \begin{Bmatrix} \frac{\Sigma_0}{R_0} \\ 1 \end{Bmatrix} \tag{64}$$

On the other hand, the normal vector to the yield surface in the augmented stress space may be expressed by the following equation:

$$\mathbf{n} = \frac{\mathbf{X}^{\mathrm{s}}}{X^0} \tag{65}$$

4.3 Updating the radius of the yield surface

As the radius of the yield surface is a function of the proportionality factor γ, this parameter must be updated. To satisfy the consistency condition with the yield surface, γ must be updated with the use of equation (45). This means that the integrating factor X^0, which is resulted at the end of a time step, is used to calculate the parameter γ at the beginning of the next step. Whenever the radius of the yield surface changes, i.e. $\bar{b} \neq 0$, equation (45) is a nonlinear equation and must be solved with numerical techniques. Utilizing equation (20), a near approximation of γ in the general time step t_{n+1} can be achieved by the following relation:

$$\gamma_{n+1}^{\mathrm{ap}} = \gamma_n + \frac{2G(\mathbf{n}_n^{\mathrm{T}} \Delta \mathbf{e})}{2\bar{G} + \bar{b}(R_{\mathrm{s}} + R_0 - R_n) - \mathbf{n}_n^{\mathrm{T}} \sum_{i=1}^{m} A_{n,i} \boldsymbol{\alpha}_{n,i}} \tag{66}$$

Since $\gamma_{n+1}^{\mathrm{ap}}$ is a neighboring value of γ_{n+1}, the perturbation method is useful in obtaining a near exact solution. The Newton-Raphson procedure gives:

$$\gamma_{n+1}^{k+1} = \gamma_{n+1}^{k} - \frac{f(\gamma_{n+1}^{k})}{f'(\gamma_{n+1}^{k})} \tag{67}$$

In this equation, k is the counter for iteration. The functions $f(\gamma_{n+1}^{k})$ and $f'(\gamma_{n+1}^{k})$ (where, $f' = \mathrm{d}f/\mathrm{d}\gamma$) can be calculated by equation (45) as follows:

$$f(\gamma_{n+1}^{k}) = \exp(-\bar{b}\gamma_{n+1}^{k}) \left[h(\gamma_{n+1}^{k})\right]^{1/\beta} - X_{n+1}^{0} \tag{68}$$

$$f'(\gamma_{n+1}^{k}) = \frac{\bar{b}(R_{\mathrm{s}} + R_0)}{\beta R_0} \left[h(\gamma_{n+1}^{k})\right]^{(1/\beta)-1} - \bar{b} \ \exp(-\bar{b}\gamma_{n+1}^{k}) \left[h(\gamma_{n+1}^{k})\right]^{1/\beta} \tag{69}$$

where:

$$h(\gamma_{n+1}^{k}) = \frac{(R_0 + R_{\mathrm{s}}) \ \exp(\bar{b}\gamma_{n+1}^{k}) - R_{\mathrm{s}}}{R_0} \tag{70}$$

The above algorithm has a second-order convergence and only a few iterations might be required to obtain a near exact solution. Consequently, using equation (12), the radius of the yield surface can be updated as follows:

$$R_{n+1} = R_0 + R_{\mathrm{s}}[1 - \exp(-\bar{b}\gamma_{n+1})] \tag{71}$$

Note that the iteration begins with $\gamma_{n+1}^{0} = \gamma_{n+1}^{\mathrm{ap}}$ as an initial value. In addition, whenever the material is saturated, i.e. $\bar{b} = 0$, γ_{n+1} can be obtained by the following closed-form solution:

$$\gamma_{n+1} = \frac{R_0}{2\bar{G}} \ln\left(X_{n+1}^{0}\right) \tag{72}$$

4.4 Updating the center of the yield surface

Since the kinematic hardening mechanism is existed, the back stress must be updated in the plastic phase. Updating the center of the yield surface is one of the important parts of the numerical solution in a plasticity problem, and it has the extra effect on accuracy of results. In this section, the augmented stress vector at the end of a time step, i.e. $\mathbf{X}_{n+1}$, is used to calculate the back stress vector at the beginning of the next step. In general, the following relation provides the exact updated components of the back stress vector:

$$\boldsymbol{\alpha}_{n+1,i} - \boldsymbol{\alpha}_{n,i} = \int_{t_n}^{t_{n+1}} (H_{\mathrm{kin},i}\dot{\mathbf{e}}^{\mathrm{p}} - \dot{\gamma}A_i\boldsymbol{\alpha}_i)\mathrm{d}t \tag{73}$$

In each time step, the last equation has three parameters, $\dot{\mathbf{e}}^{\mathrm{p}}$, A_i and $\boldsymbol{\alpha}_i$, which are all time variables (except for the parameter A_i in equation (14) for Chaboche model). Here, it is assumed that A_i is constant throughout each time step with its value at the start of time step, $A_{n,i}$. Also, α_i may be approximated by an average of its value at the start and end of the time step, i.e. $\boldsymbol{\alpha}_i = 1/2(\boldsymbol{\alpha}_{n,i} + \boldsymbol{\alpha}_{n+1,i})$. Thus, equation (73) can be expressed as follows:

$$\boldsymbol{\alpha}_{n+1,i} - \boldsymbol{\alpha}_{n,i} = H_{\mathrm{kin},i}\int_{t_n}^{t_{n+1}} \dot{\mathbf{e}}^{\mathrm{p}}\mathrm{d}t - A_{n,i}\frac{(\boldsymbol{\alpha}_{n,i} + \boldsymbol{\alpha}_{n+1,i})}{2}\int_{t_n}^{t_{n+1}} \dot{\gamma}\mathrm{d}t \tag{74}$$

$$\boldsymbol{\alpha}_{n+1,i} - \boldsymbol{\alpha}_{n,i} = H_{\mathrm{kin},i}\Delta\mathbf{e}^{\mathrm{p}} - \frac{\lambda}{2}A_{n,i}(\boldsymbol{\alpha}_{n,i} + \boldsymbol{\alpha}_{n+1,i}) \tag{75}$$

where, λ is defined by $\lambda = \gamma_{n+1} - \gamma_n$. By some manipulations, the last equation may be converted to:

$$\boldsymbol{\alpha}_{n+1,i} = \frac{1}{2 + \lambda A_{n,i}}\left[2H_{\mathrm{kin},i}\Delta\mathbf{e}^{\mathrm{p}} + (2 - \lambda A_{n,i})\boldsymbol{\alpha}_{n,i}\right] \tag{76}$$

Now, the center of the yield surface can be obtained by the next relationship:

$$\boldsymbol{\alpha}_{n+1} = \bar{H}_{\mathrm{kin}}\Delta\mathbf{e}^{\mathrm{p}} + \mathbf{a} \tag{77}$$

where:

$$\bar{H}_{\mathrm{kin}} = \sum_{i=1}^{m} \frac{2H_{\mathrm{kin},i}}{2 + \lambda A_i} \tag{78}$$

$$\mathbf{a} = \sum_{i=1}^{m} \frac{2 - \lambda A_{n,i}}{2 + \lambda A_{n,i}}\boldsymbol{\alpha}_{n,i} \tag{79}$$

Note that the increment of the deviatoric plastic strain in equation (77) is unknown. Using equations (2) and (7), the following equation at time t_{n+1} is achieved:

$$\boldsymbol{\Sigma}_{n+1} = \mathbf{s}_n + 2G(\Delta\mathbf{e} - \Delta\mathbf{e}^{\mathrm{p}}) - \boldsymbol{\alpha}_{n+1} \tag{80}$$

Inserting equation (77) into equation (80) and rearranging the result, the vector $\Delta\mathbf{e}^{\mathrm{p}}$ will be obtained as:

$$\Delta\mathbf{e}^{\mathrm{p}} = \frac{1}{2G + \bar{H}_{\mathrm{kin}}}(\mathbf{s}_n + 2G\Delta\mathbf{e} - \mathbf{a} - \Sigma_{n+1}) \tag{81}$$

Finally, referring to equations (76) and (77), the back stress vector and its components are completely determined. Moreover, the shifted stress at time t_{n+1} can be obtained by the following equation:

$$\Sigma_{n+1} = \frac{\mathbf{X}^{\mathrm{s}}_{n+1}}{X^{0}_{n+1}} R_{n+1} \tag{82}$$

4.5 General elastic-plastic load steps

Following a standard methodology, a predictor-corrector algorithm can be used for integration process. Here, a general load step begins by calculating an elastic trial value in the augmented stress space as follows:

$$\mathbf{X}^{\mathrm{TR}}_{n+1} = \mathbb{G}^{\mathrm{e}}\mathbf{X}_n \tag{83}$$

Now, the trail estimation must be checked to be acceptable, i.e.:

$$\|\mathbf{X}^{\mathrm{s,TR}}_{n+1}\| \leq X^{0,\mathrm{TR}}_{n+1} \tag{84}$$

If this condition is satisfied, then the load step is in the elastic phase, and the final solution is equal to $\mathbf{X}^{\mathrm{TR}}_{n+1}$. Otherwise, the load step is an elastic-plastic one. Consequently, the elastic part of the load step may be separated from the plastic part by means of the scalar parameter α, which is introduced in equation (24) but with the following definition for parameters C, D and M in the augmented stress space:

$$D = \left(\frac{2G}{R_n} X^{0}_{n} \|\Delta\mathbf{e}\|\right)^2, \quad C = \frac{2G}{R_n} X^{0}_{n} \left(\mathbf{X}^{\mathrm{s}}_{n}\right)^{\mathrm{T}} \Delta\mathbf{e}, \quad M = \|\mathbf{X}^{\mathrm{s}}_{n}\|^2 - \left(X^{0}_{n}\right)^2 \tag{85}$$

Using the parameter α, the augmented stress vector of the contact point can be computed by the following equation:

$$\mathbf{X}^{\mathrm{c}} = \mathbb{G}^{\mathrm{c}}\mathbf{X}_n \tag{86}$$

Utilizing equation (61), the matrix $\mathbb{G}^{\mathrm{c}}$ is obtained by:

$$\mathbb{G}^{\mathrm{c}} = \begin{bmatrix} \mathbb{I}_{9\times 9} & \frac{2G}{R_n}\alpha\Delta\mathbf{e} \\ \mathbf{0}^{\mathrm{T}} & 1 \end{bmatrix} \tag{87}$$

Since $(1 - \alpha)\Delta\mathbf{e}$ denotes a fully plastic step, the updated augmented stress at the end of the load step can still be computed by equation (62) with the following modifications:

$$g = \frac{2G}{R_n}\|(1 - \alpha)\Delta\mathbf{\Phi}\| \tag{88}$$

$$\Delta\boldsymbol{\Phi} = \Delta\mathbf{e} + \frac{(\mathbf{n}^{\mathrm{c}})^{\mathrm{T}}\Delta\mathbf{e}}{2\bar{G} + \bar{b}(R_{\mathrm{s}} + R_0 - R_n) - (\mathbf{n}^{\mathrm{c}})^{\mathrm{T}}\sum_{i=1}^{m} A_i^{\mathrm{c}}\boldsymbol{\alpha}_{n,i}} \sum_{i=1}^{m} A_i^{\mathrm{c}}\boldsymbol{\alpha}_{n,i} \tag{89}$$

In the above equation, A_i^{c} and $\mathbf{n}^{\mathrm{c}}$ are the values at the contact point, i.e. $A_i^{\mathrm{c}} = A_i(\boldsymbol{\alpha}_n, \mathbf{n}^{\mathrm{c}})$, and $\mathbf{n}^{\mathrm{c}}$ may be expressed as follows:

$$\mathbf{n}^{\mathrm{c}} = \frac{\mathbf{X}_{n+1}^{\mathrm{s,c}}}{X_{n+1}^{0,\mathrm{c}}}, \quad \mathbf{X}^{\mathrm{c}} = \begin{Bmatrix} \mathbf{X}_{n+1}^{\mathrm{s,c}} \\ X_{n+1}^{0,\mathrm{c}} \end{Bmatrix} \tag{90}$$

4.6 Discrete consistent tangent matrix

By linearizing the discrete time procedure, as it was done in Section 3.2, the elastoplastic consistent tangent matrix can be developed. Here, equation (31) can be used as a relation for the discrete consistent operator, and only the terms $(\partial\boldsymbol{\Sigma}/\partial\mathbf{e})_{n+1}$ and $(\partial\boldsymbol{\alpha}/\partial\mathbf{e})_{n+1}$ must be determined. Taking the derivative with respect to $\mathbf{e}_{n+1}$ from equation (82), leads to the next relation:

$$\begin{aligned} \frac{\partial\boldsymbol{\Sigma}_{n+1}}{\partial\mathbf{e}_{n+1}} = \frac{R_{n+1}}{X_{n+1}^0}\frac{\partial\mathbf{X}_{n+1}^{\mathrm{s}}}{\partial\mathbf{e}_{n+1}} - \frac{R_{n+1}}{\left(X_{n+1}^0\right)^2}\left[\mathbf{X}_{n+1}^{\mathrm{s}}\left(\frac{\partial X_{n+1}^0}{\partial\mathbf{e}_{n+1}}\right)^{\mathrm{T}}\right] \\ + \frac{1}{X_{n+1}^0}\left[\mathbf{X}_{n+1}^{\mathrm{s}}\left(\frac{\partial R_{n+1}}{\partial\mathbf{e}_{n+1}}\right)^{\mathrm{T}}\right] \end{aligned} \tag{91}$$

The derivatives that are appeared in the last equation are very complicated, and they are fully addressed in Appendix 3. Finally, the derivative $(\partial\boldsymbol{\alpha}/\partial\mathbf{e})_{n+1}$ will be determined by utilizing equation (77) as follows:

$$\frac{\partial\boldsymbol{\alpha}_{n+1}}{\partial\mathbf{e}_{n+1}} = \Delta\mathbf{e}^{\mathrm{p}}\left(\frac{\partial\bar{H}_{\mathrm{kin}}}{\partial\mathbf{e}_{n+1}}\right)^{\mathrm{T}} + \bar{H}_{\mathrm{kin}}\frac{\partial\Delta\mathbf{e}^{\mathrm{p}}}{\partial\mathbf{e}_{n+1}} + \frac{\partial\mathbf{a}}{\partial\mathbf{e}_{n+1}} \tag{92}$$

The derivatives of the parameters $\bar{H}_{\mathrm{kin}}$, $\Delta\mathbf{e}^{\mathrm{p}}$ and $\mathbf{a}$ are computed with the use of equations (78), (79) and (81), respectively. The results are presented by the following equations:

$$\frac{\partial\bar{H}_{\mathrm{kin}}}{\partial\mathbf{e}_{n+1}} = -\sum_{i=1}^{m}\frac{2\lambda H_{\mathrm{kin},i}}{\left(2 + \lambda A_i^{\mathrm{c}}\right)^2}\frac{\partial A_i^{\mathrm{c}}}{\partial\mathbf{e}_{n+1}} - \sum_{i=1}^{m}\frac{2A_i^{\mathrm{c}}H_{\mathrm{kin},i}}{\left(2 + \lambda A_i^{\mathrm{c}}\right)^2}\frac{\partial\lambda}{\partial\mathbf{e}_{n+1}} \tag{93}$$

$$\begin{aligned} \frac{\partial\mathbf{a}}{\partial\mathbf{e}_{n+1}} = -\sum_{i=1}^{m}\frac{4\lambda}{\left(2 + \lambda A_i^{\mathrm{c}}\right)^2}\left[\boldsymbol{\alpha}_{n,i}\left(\frac{\partial A_i^{\mathrm{c}}}{\partial\mathbf{e}_{n+1}}\right)^{\mathrm{T}}\right] \\ - \sum_{i=1}^{m}\frac{4A_i^{\mathrm{c}}}{\left(2 + \lambda A_i^{\mathrm{c}}\right)^2}\left[\boldsymbol{\alpha}_{n,i}\left(\frac{\partial\lambda}{\partial\mathbf{e}_{n+1}}\right)^{\mathrm{T}}\right] \end{aligned} \tag{94}$$

$$\frac{\partial \Delta \mathbf{e}^{\mathrm{p}}}{\partial \mathbf{e}_{n+1}} = -\frac{1}{\left(2G + \bar{H}_{\mathrm{kin}}\right)^2}(\mathbf{s}_n + 2G\Delta\mathbf{e} - \mathbf{a} - \Sigma_{n+1}) \times \left(\frac{\partial \bar{H}_{\mathrm{kin}}}{\partial \mathbf{e}_{n+1}}\right)^{\mathrm{T}} + \frac{1}{2G + \bar{H}_{\mathrm{kin}}}\left(2G\mathbb{I} - \frac{\partial \mathbf{a}}{\partial \mathbf{e}_{n+1}} - \frac{\partial \Sigma_{n+1}}{\partial \mathbf{e}_{n+1}}\right) \tag{95}$$

Finally, the derivatives of the parameters A_i^{c} and λ are presented in Appendixes 1 and 3, respectively.

5. Numerical examples

An incremental nonlinear finite element analysis has two major algorithms. The first one, which is normally Newton like, is used for solving nonlinear simultaneous equations. This process needs tangential stiffness matrix of structure for rapid convergence and a tangent operator, i.e. $\partial\boldsymbol{\sigma}/\partial\boldsymbol{\varepsilon}$, at each Gauss point of every element must be calculated. The other one is the integration algorithm and is used to determine the stress increment corresponding to a strain increment. The integration procedure must be performed at every Gauss point for each load step, and also, their corrective iterations. The tangent operator in the first algorithm must be consistent with the integration scheme of the second one.

This study is focused on the integration scheme, and all numerical presentations are point-wise. The robustness and performance of the new exponential-based integration method are investigated by many numerical tests in this section. The results of the suggested technique are compared with the responses of the classical forward Euler, which was presented in detail in Section 3. The numerical examples are classified in three categories. First, the piecewise strain load histories with different time steps are considered, and the relative errors along with the average error of the stress outputs are plotted. In other words, the accuracy and the rate of convergence of the new stress-updating algorithm are studied. Second, to explore the validity of the consistent tangent operator, the input stress load histories with a variety of the time steps are assumed and the relative error and the average error of the strain outputs are shown. Third, the error contour plots for different states and the piecewise mixed stress-strain load histories are presented. This is an efficient tool to explore the accuracy of an integration scheme in plasticity.

Since the exact solutions of the investigated problems are not available, the results of the forward Euler algorithm with very fine time steps ($\Delta t = 1 \times 10^{-5}$ s) are assumed to be the exact solutions. The material is considered as aluminum 7050-T7451 that is used for the aft fuselage stub frames on F/A-18 fighter planes (Hu *et al.*, 1999). The material has the Young's modulus of $E = 69$ GPa (10,000 ksi) and the Poisson's ratio of $\nu = 0.33$. Its mechanical characteristics for the isotropic hardening are as follows:

$$R_0 = 328\,\mathrm{MPa}, \quad R_{\mathrm{s}} = 25\,\mathrm{MPa}, \quad \bar{b} = 10$$

Moreover, the mechanical properties of the kinematic hardening rule for the Chaboche model-3 decomposed rule are as follows:

$$H_{\mathrm{kin},1} = 63,930\,\mathrm{MPa}, \quad H_{\mathrm{nl},1} = 734$$

$$H_{\mathrm{kin},2} = 9,980\,\mathrm{MPa}, \quad H_{\mathrm{nl},2} = 728$$

$$H_{\text{kin},3} = 6,620\,\text{MPa}, \quad H_{\text{nl},3} = 73$$

5.1 Strain-controlled histories

Two non-proportional strain-controlled histories are adopted. All other strain components are considered equal to zero. The strain components are assumed to change proportionally to the strain value of the first yielding of the uniaxial loading state, i.e. $\varepsilon_{y0} = \sqrt{3/2}(R_0/E)$. Updated stress histories are computed with the new exponential-based formulation and also the forward Euler method for the sake of comparison. The results are obtained using three practical load step sizes ($\Delta t = 0.0500$, 0.0250, 0.0125 s). The non-dimensional or relative error of the updated stresses is introduced as stress relative error by the following equation:

$$E_n^{\sigma} = \frac{\|\boldsymbol{\sigma}_n - \boldsymbol{\sigma}_n^*\|}{R_n} \tag{96}$$

In the last equation, $\boldsymbol{\sigma}_n^*$ denotes the exact stress at time t_n. Also, $\boldsymbol{\sigma}_n$ and R_n are the stress vector and the yield surface radius pertaining to the practical load step at the time t_n. In order to investigate the rate of convergence of the new integration method, the average stress error of the updated stresses is defined by:

$$E_{\text{T}}^{\sigma} = \frac{1}{N}\sum_{n=1}^{N} \frac{\|\boldsymbol{\sigma}_n - \boldsymbol{\sigma}_n^*\|}{R_n} \tag{97}$$

where, N is the total number of the load steps. By adopting different size of load steps, the average error is computed for both strategies and the results are plotted in a logarithmic space.

Figures 1 and 2 show the strain-controlled history 1 and its path, respectively. The stress relative error of the new scheme and the forward Euler algorithm are shown in Figures 3-5. Figure 6 shows the average stress error for these techniques. For a better demonstration of the performance of the proposed integration formulation, another strain

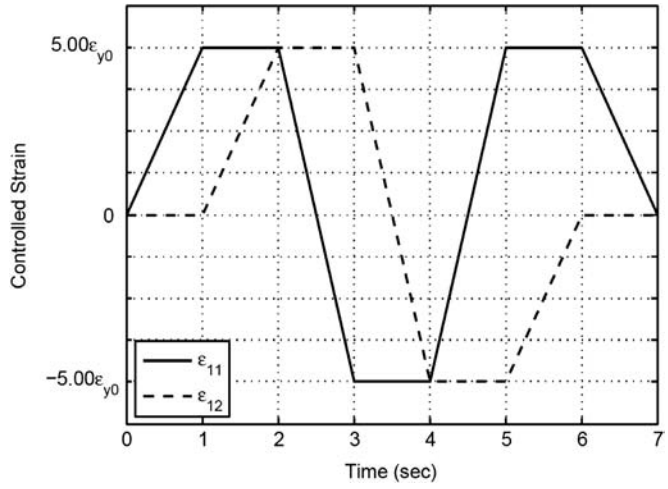

Figure 1.
Strain-controlled history 1

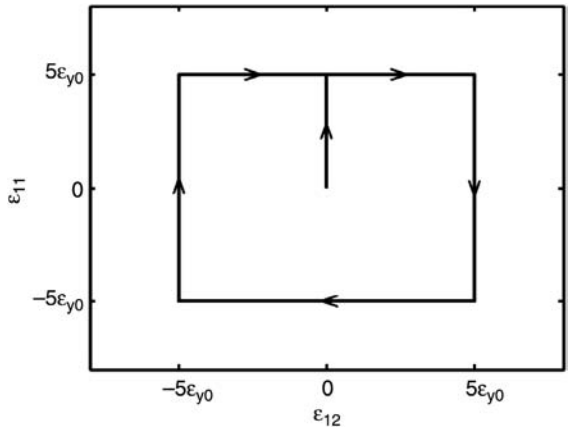

Figure 2.
Strain path 1

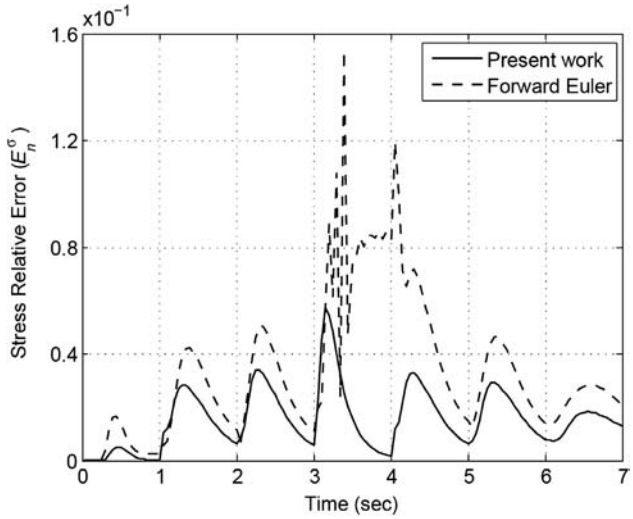

Note: Δt = 0.0500 s

Figure 3.
Stress relative error of strain path 1

history is considered. The strain-controlled history 2 and its path are shown in Figures 7 and 8, respectively. The stress relative error of the suggested procedure in comparison with the forward Euler method is shown in Figures 9 through 11. Figure 12 shows the rate of the convergence of the average stress error for these procedures. The related diagrams show that the accuracy of the present work is much better than the classical forward Euler one. Another finding is the linear rate of the convergence of the new integration algorithm, which is illustrated by the diagrams of the average stress error.

For a convincible demonstration, the formulation of backward Euler method, which is an implicit algorithm and was presented comprehensively by Kobayashi and Ohno (2002), is also tested. The stresses for strain path 1 and 2 are updated by backward Euler scheme with different time step sizes. Since the errors of the forward and

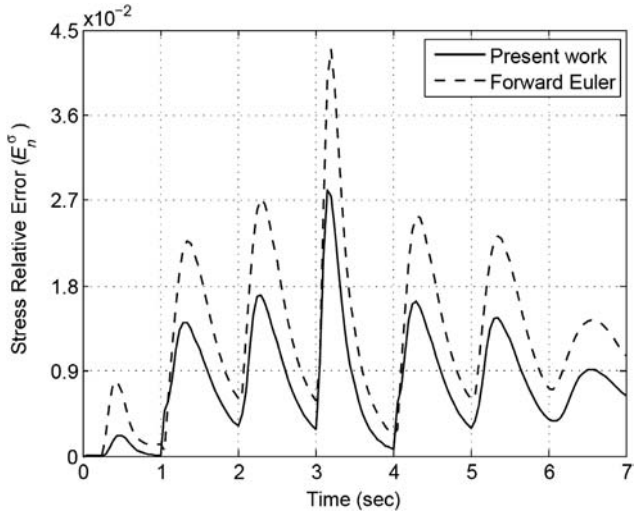

Note: $\Delta t = 0.0250$ s

Figure 4.
Stress relative error of strain path 1

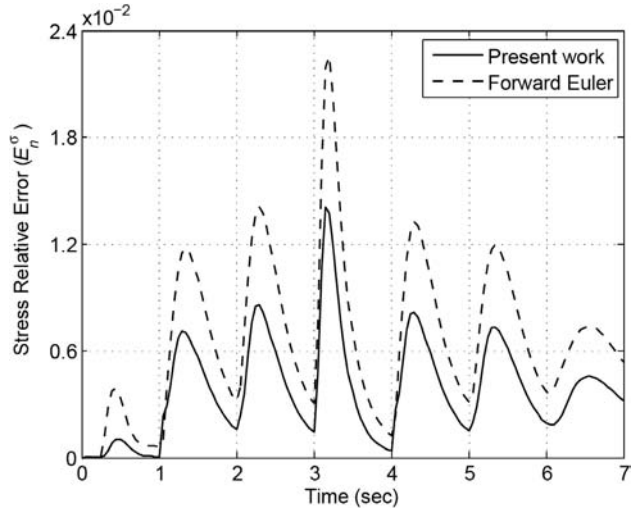

Note: $\Delta t = 0.0125$ s

Figure 5.
Stress relative error of strain path 1

backward Euler are very close, the results are presented in the tabulated form. Tables I and II give average errors for strain path 1 and 2, respectively. These show that the new presented integration method significantly improves accuracy.

At this stage, it is intended to compare the efficiency of three different integration algorithms. Here, efficiency is given by the following definition:

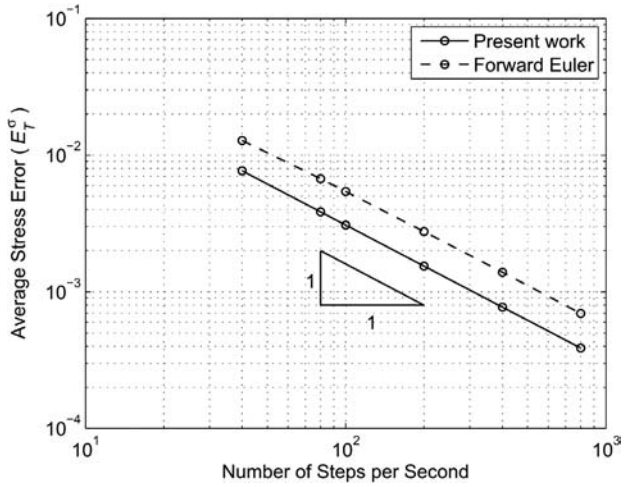

Figure 6.
Average stress error of strain path 1

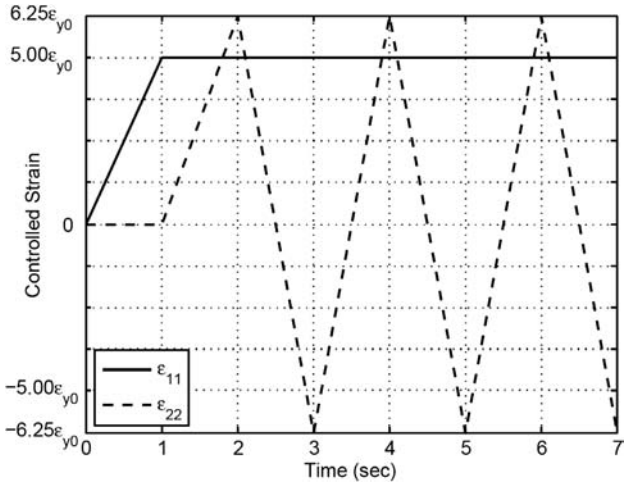

Figure 7.
Strain-controlled history 2

$$\text{Efficiency} = \frac{\text{Accuracy}}{\text{Computational effort}} = \frac{1}{\text{CPU time (s)} \times \text{Average error (\%)}} \tag{98}$$

It is of great importance for finite element applications. In a point-wise problem, the computation time on a normal CPU is very short. To give a measurable CPU time, the strain history 1 in Figure 1 is repeated 150 times with a total time of 1,050 s. Time step size is considered as $\Delta t = 0.0250$ (s) and average errors based on equation (97) are computed. For a better demonstration, efficiencies are normalized with respect to the efficiency of exponential maps method. Results presented in Table III show the superior efficiency of the new integration algorithm.

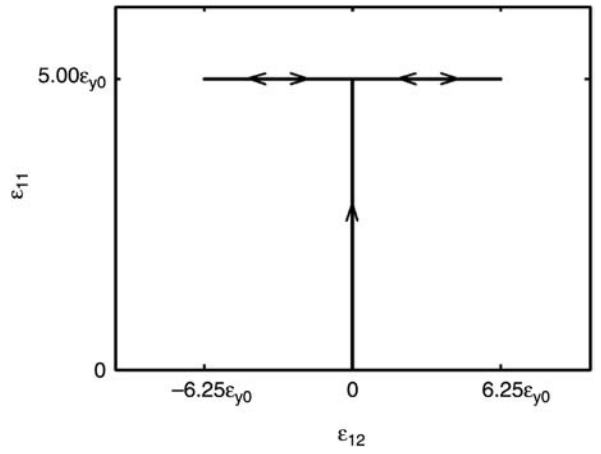

Figure 8.
Strain path 2

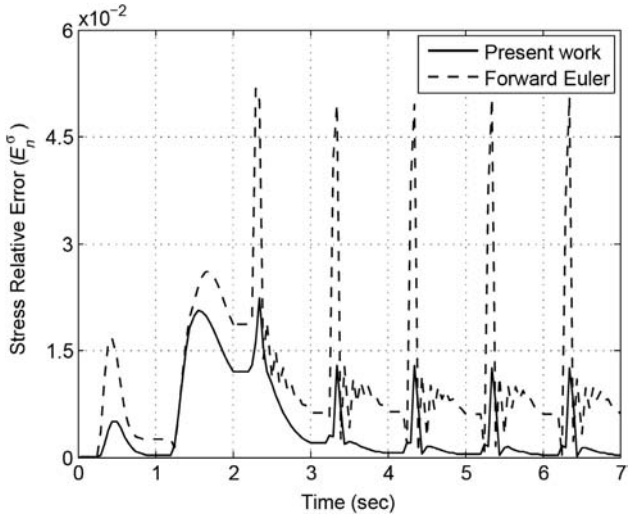

Figure 9.
Stress relative error of strain path 2

Note: $\Delta t = 0.0500$ s

5.2 Stress-controlled histories

In these point-wise problems, the objective is to test the second-order convergence rate of the elastoplastic consistent tangent through a Newton algorithm in a load-driven manner with the iterative process. Two non-proportional stress-controlled histories are considered. All other stress components are assumed zero. The stress components are varied proportionally to the stress value of the first yielding of the uniaxial loading state, i.e. σ_{y0}. The strain histories are updated with the exponential-based method and with the forward Euler algorithm. The results are reported by three practical load step sizes ($\Delta t = 0.0500, 0.0250, 0.0125$ s). The strain relative error of the updated strains can be defined by the following equation:

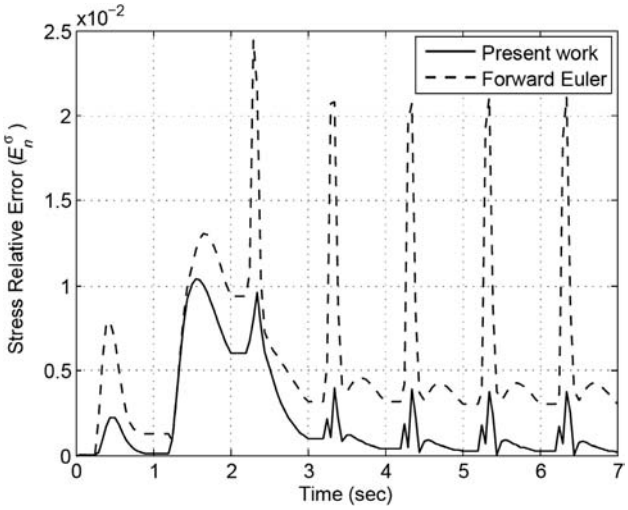

Note: $\Delta t = 0.0250$ s

Figure 10.
Stress relative error of strain path 2

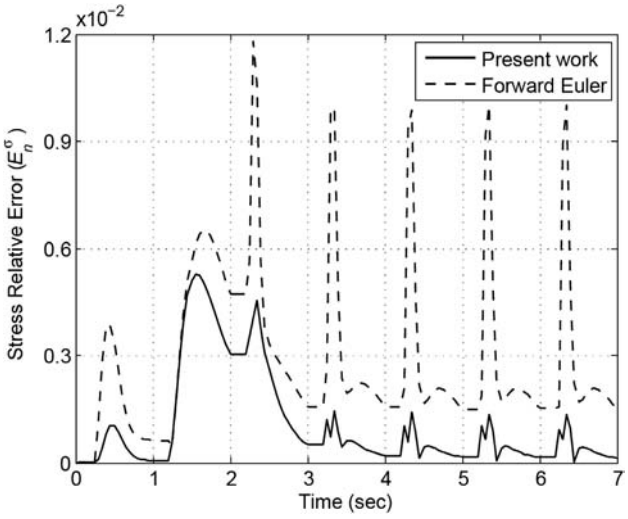

Note: $\Delta t = 0.0125$ s

Figure 11.
Stress relative error of strain path 2

$$E_n^{\varepsilon} = 2G\frac{\|\boldsymbol{\varepsilon}_n - \boldsymbol{\varepsilon}_n^*\|}{R_n} \tag{99}$$

where, $\boldsymbol{\varepsilon}_n^*$ is the exact strain vector at time t_n. Also, $\boldsymbol{\varepsilon}_n$ and R_n are calculated by the numerical solutions with practical time steps. The average strain error of the updated strain vectors is defined by the following equation:

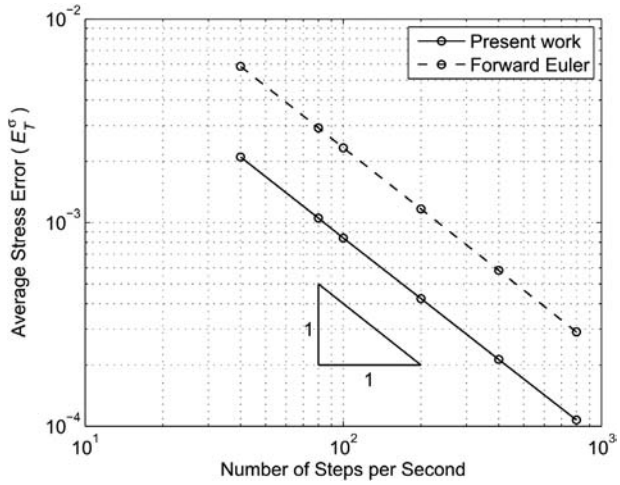

Figure 12.
Average stress error of strain path 2

Size of time step (s)	Present work	Forward Euler	Backward Euler
0.0500	1.555	3.357	2.646
0.0250	0.769	1.279	1.377
0.0125	0.385	0.672	0.704

Table I.
Average error (%) by different algorithms for strain path 1

Size of time step (s)	Present work	Forward Euler	Backward Euler
0.0500	0.431	1.146	1.083
0.0250	0.210	0.586	0.573
0.0125	0.105	0.292	0.291

Table II.
Average error (%) by different algorithms for strain path 2

Algorithm	Average error (%)	CPU time (s)	Efficiency	Normalized efficiency
Exponential maps (present study)	0.84	8.27	0.1440	1
Forward Euler (present study)	1.38	6.79	0.1067	0.74
Backward Euler (Kobayashi and Ohno, 2002)	1.46	13.65	0.0501	0.35

Note: $\Delta t = 0.025\,\mathrm{s}$

Table III.
Efficiency of the algorithms for 150 cycles of the strain path 1

$$E_{\mathrm{T}}^{\boldsymbol{\varepsilon}} = \frac{1}{N}\sum_{n=1}^{N} 2G\frac{\|\boldsymbol{\varepsilon}_n - \boldsymbol{\varepsilon}_n^*\|}{R_n} \tag{100}$$

The stress-controlled history 1 and its path are shown in Figures 13 and 14, respectively. The accuracies of the new formulation, in comparison with forward Euler method, are shown in Figures 15 through 17. The average strain error for the stress

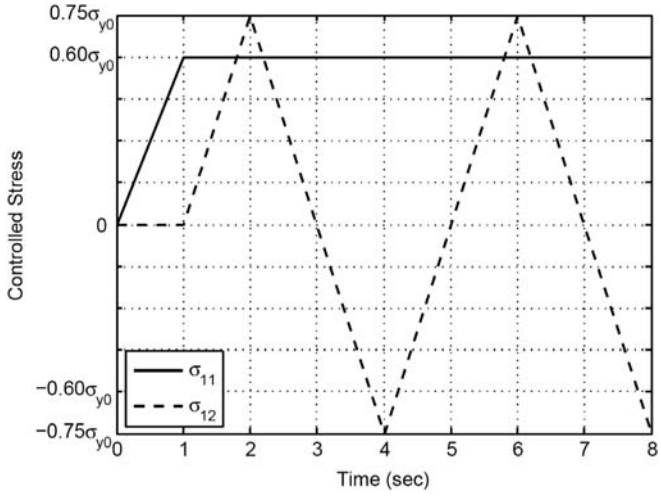

Figure 13.
Stress-controlled history 1

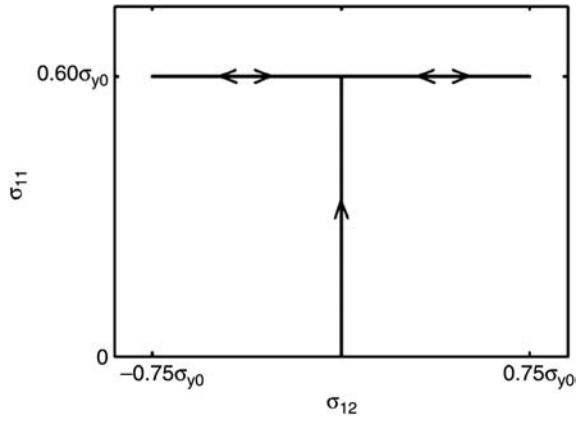

Figure 14.
Stress path 1

history 1 is illustrated in a logarithmic space in Figure 18. The stress-controlled history 2 and its path are shown in Figures 19 and 20, respectively. The strain relative errors for the new technique and also for forward Euler strategy are shown in Figures 21 through 23. Moreover, its average strain error is shown in Figure 24.

The diagrams of the stress-controlled histories demonstrate robustness of the new technique versus the classical forward Euler method. Furthermore, the average strain error diagrams illustrate the first-order convergence for both the classical forward Euler and the exponential-based approaches.

To examine the rate of convergence, the relative Euclidean norms of error in the Newton iterations for each time step are defined by the following relation:

$$E_n^i = \frac{\left\|\boldsymbol{\varepsilon}_n^i - \boldsymbol{\varepsilon}_n\right\|}{\left\|\boldsymbol{\varepsilon}_n^1 - \boldsymbol{\varepsilon}_n\right\|} \tag{101}$$

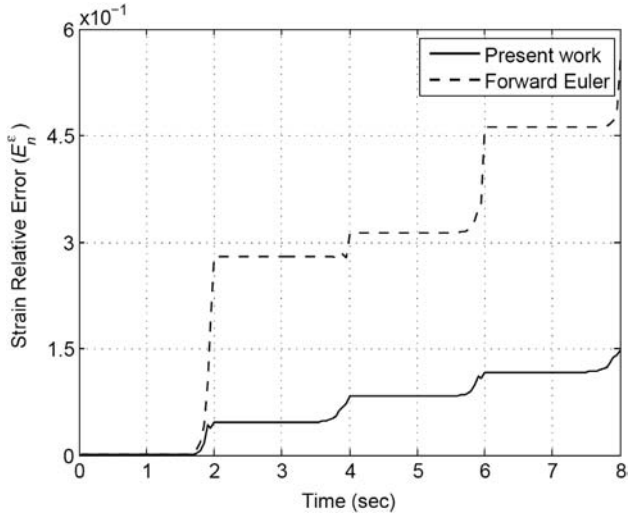

Note: $\Delta t = 0.0500$ s

Figure 15.
Strain relative error of stress path 1

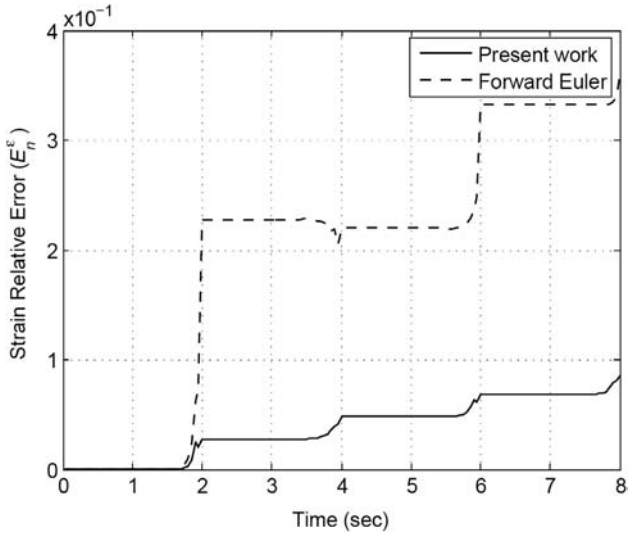

Note: $\Delta t = 0.0250$ s

Figure 16.
Strain relative error of stress path 1

where, $\boldsymbol{\varepsilon}_n$ and $\boldsymbol{\varepsilon}_n^i$ are the converged strain and its ith estimation in time t_n, respectively. To demonstrate the second-order convergence of tangent operators, the relative Euclidean norms, E_n^i, for successive iterations in two arbitrary times, are presented in Tables IV and V for stress path 1 and 2, respectively. These tables show the second-order convergence rate of the elastoplastic consistent tangent operator.

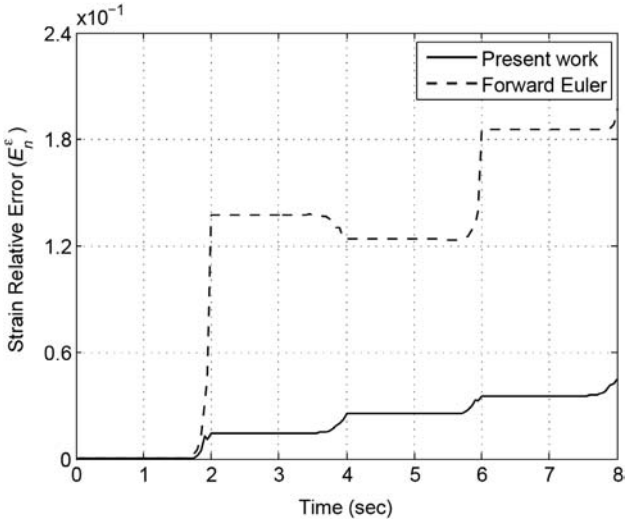

Note: $\Delta t = 0.0125$ s

Figure 17.
Strain relative error of stress path 1

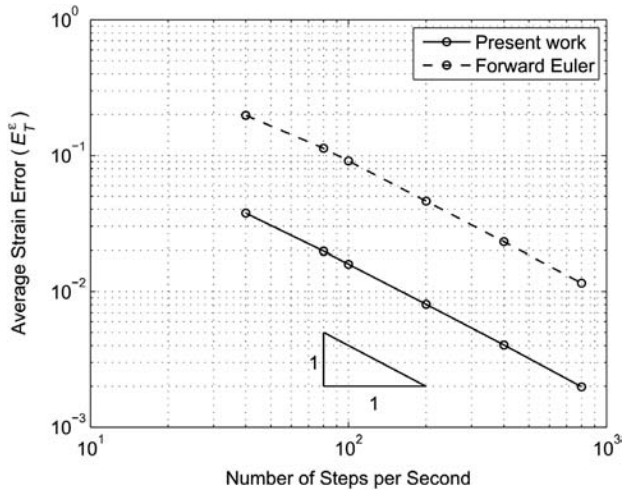

Figure 18.
Average strain error of stress path 1

5.3 Error contour plots

To examine the integration accuracy of the elastic-perfectly plastic von-Mises model, the error contour plots, or iso-error maps, were first presented by Krieg and Krieg (1977). Subsequently, the iso-error maps were used by Ortiz and Popov (1985), Ortiz and Simo (1986), Simo and Hughes (1998), Artioli *et al.* (2006, 2007) and Rezaiee-Pajand and Nasirai (2008). In this study, by considering a plane stress state, three different positions of the stress point on the yield surface are adopted for starting points. The positions are corresponded to uniaxial, biaxial and pure shear, which are labeled A, B and C in Figure 25, respectively. Afterward, to obtain error contour plots, by controlling

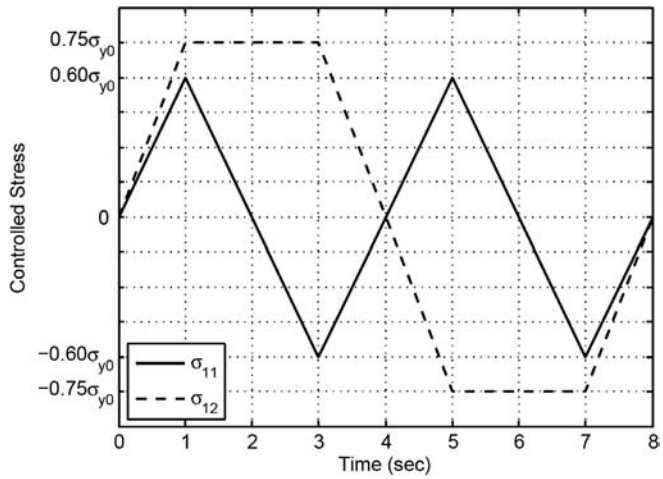

Figure 19.
Stress-controlled history 2

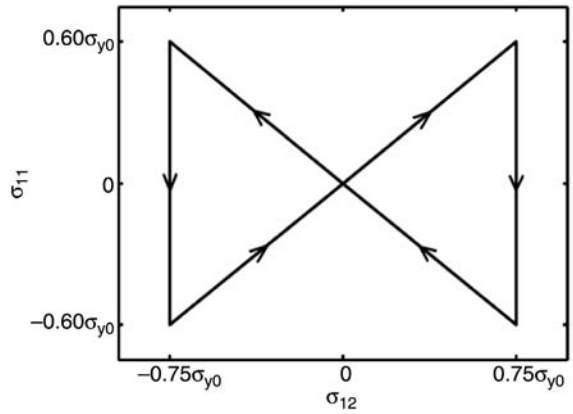

Figure 20.
Stress path 2

the strain increments $\Delta\varepsilon_{11}$ and $\Delta\varepsilon_{22}$, a purely plastic step is considered, while keeping all the remaining stresses zero. In the following, the strain increments for ε_{11} and ε_{22} components are selected from zero to $2\varepsilon_{11}^{y,0}$ and $2\varepsilon_{22}^{y,0}$, respectively:

$$\frac{\Delta\varepsilon_{11}}{\varepsilon_{11}^{y,0}} = 0, 0.05, 0.10, \ldots, 2$$

$$\frac{\Delta\varepsilon_{22}}{\varepsilon_{22}^{y,0}} = 0, 0.05, 0.10, \ldots, 2$$

The stress updating of 41×41 mixed stress-strain histories for each one of the uniaxial, biaxial and pure shear states are computed. Furthermore, for every mixed history, the percent of the error for the updated stress is calculated by the following equation:

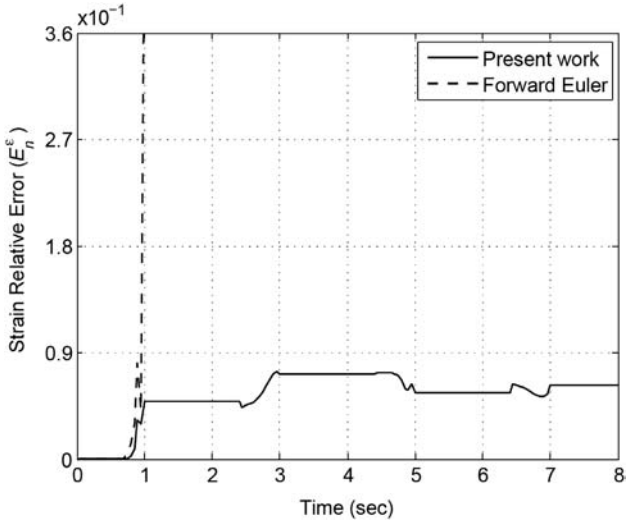

Note: $\Delta t = 0.0500$ s

Figure 21.
Strain relative error of stress path 2

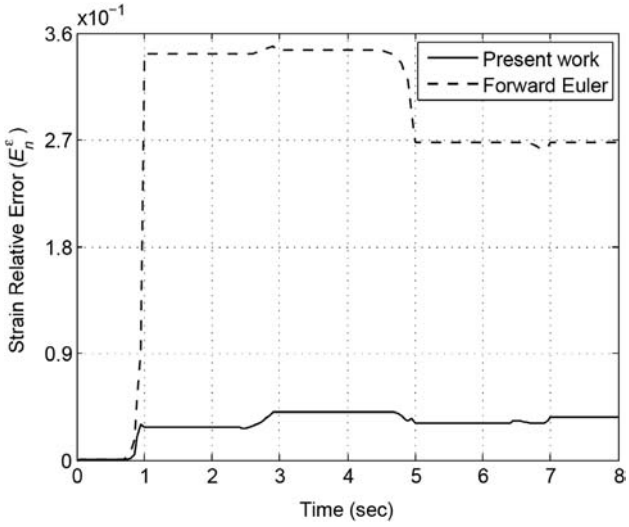

Note: $\Delta t = 0.0250$ s

Figure 22.
Strain relative error of stress path 2

$$E_{\text{iso}}^{\boldsymbol{\sigma}} = \frac{\|\boldsymbol{\sigma} - \boldsymbol{\sigma}^*\|}{\|\boldsymbol{\sigma}^*\|} \times 100\% \tag{102}$$

where, $\boldsymbol{\sigma}^*$ and $\boldsymbol{\sigma}$ are the exact stress vector and the numerical stress vector, respectively. The error contour plots for each starting state and both mentioned techniques are shown

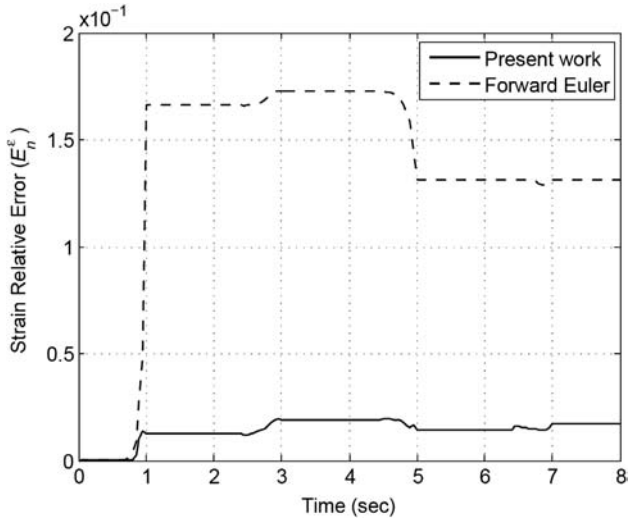

Note: $\Delta t = 0.0125$ s

Figure 23.
Strain relative error of stress path 2

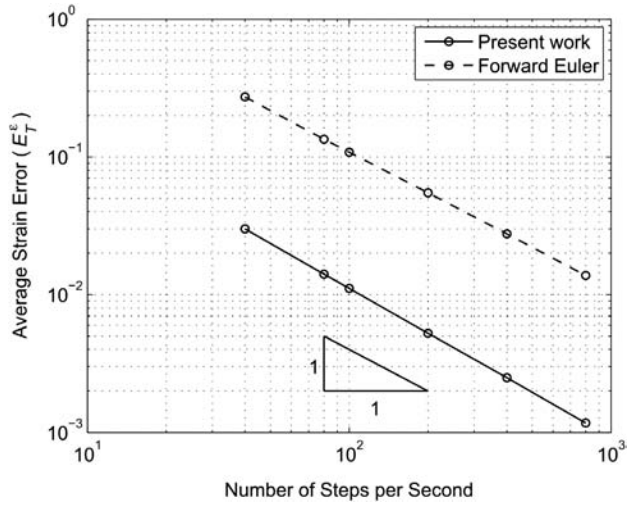

Figure 24.
Average strain error of stress path 2

in Figures 26 through 31. In all diagrams, the areas correspond to the error percentage less than 10 percent are hatched. These shaded areas show that the new presented algorithm even with large load steps gives very accurate results.

6. Conclusions

The von-Mises plasticity model in the small strain regime with a mixed nonlinear hardening mechanism is considered. An exponential formulation for the nonlinear isotropic hardening is assumed. Moreover, a class of multi-components form with

a recovery term for the nonlinear kinematic hardening is adopted. A new integration strategy based on the exponential maps for integrating the nonlinear constitutive equations is proposed. In this scheme, the updated stress satisfies automatically the condition of consistency with the yield surface. Furthermore, the discrete consistent tangent operator for the new integration technique is provided. For the forward

	$t = 4$ s		$t = 8$ s	
Iteration	Present work	Forward Euler	Present work	Forward Euler
1	$1.0000 \times 10^{+00}$	$1.0000 \times 10^{+00}$	$1.0000 \times 10^{+00}$	$1.0000 \times 10^{+00}$
2	1.0024×10^{-01}	1.2807×10^{-02}	8.4559×10^{-02}	1.2214×10^{-02}
3	2.7474×10^{-04}	1.8792×10^{-03}	6.2085×10^{-04}	1.1267×10^{-03}
4	4.0372×10^{-05}	4.0933×10^{-06}	4.4698×10^{-05}	6.0571×10^{-07}
5	3.5543×10^{-08}	1.4173×10^{-07}	7.6092×10^{-08}	4.9765×10^{-09}

Note: $\Delta t = 0.025$ s

Table IV.
Typical convergence value, the relative Euclidean norms for stress path 1

	$t = 3$ s		$t = 7$ s	
Iteration	Present work	Forward Euler	Present work	Forward Euler
1	$1.0000 \times 10^{+00}$	$1.0000 \times 10^{+00}$	$1.0000 \times 10^{+00}$	$1.0000 \times 10^{+00}$
2	9.5530×10^{-02}	1.3984×10^{-02}	8.1247×10^{-02}	1.3193×10^{-02}
3	1.5481×10^{-03}	2.2979×10^{-03}	7.7282×10^{-04}	2.3258×10^{-03}
4	5.2445×10^{-05}	1.2757×10^{-05}	2.5355×10^{-05}	1.5108×10^{-05}
5	1.8142×10^{-08}	1.3747×10^{-06}	3.0359×10^{-08}	2.0044×10^{-06}

Note: $\Delta t = 0.025$ s

Table V.
Typical convergence value, the relative Euclidean norms for stress path 2

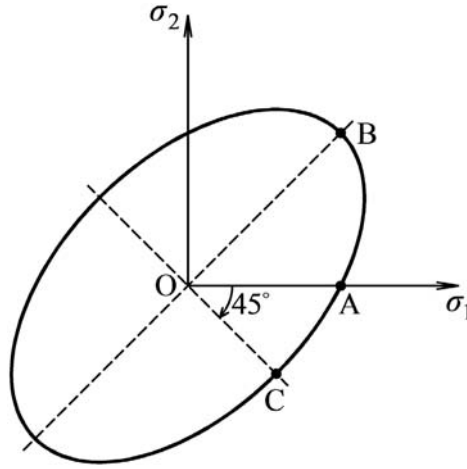

Figure 25.
Plane stress von-Mises yield surface and start points for error contour plots

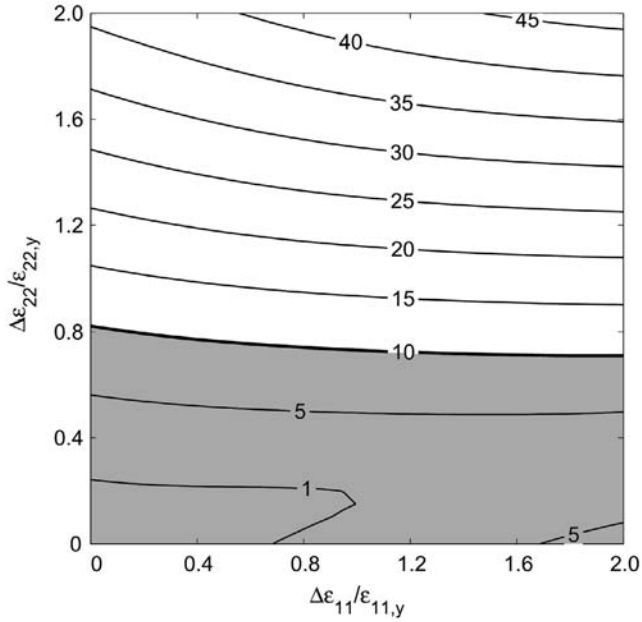

Figure 26.
Iso-error map corresponding to uniaxial state on the yield surface for the forward Euler method

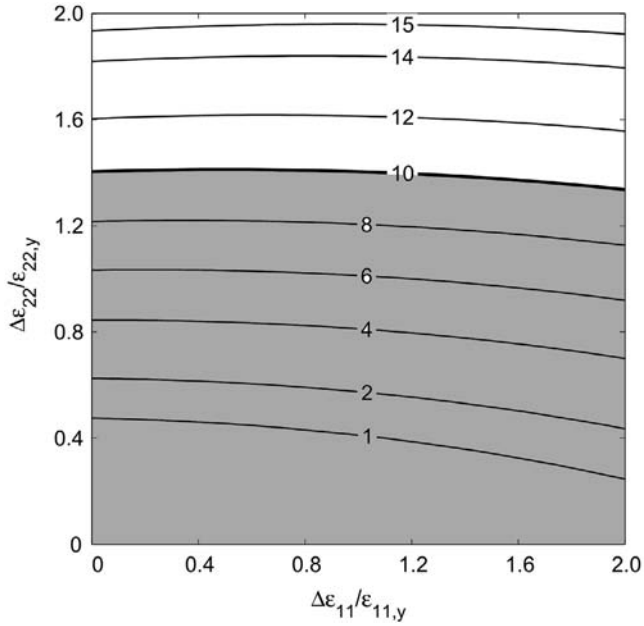

Figure 27.
Iso-error map corresponding to uniaxial state on the yield surface for the present work

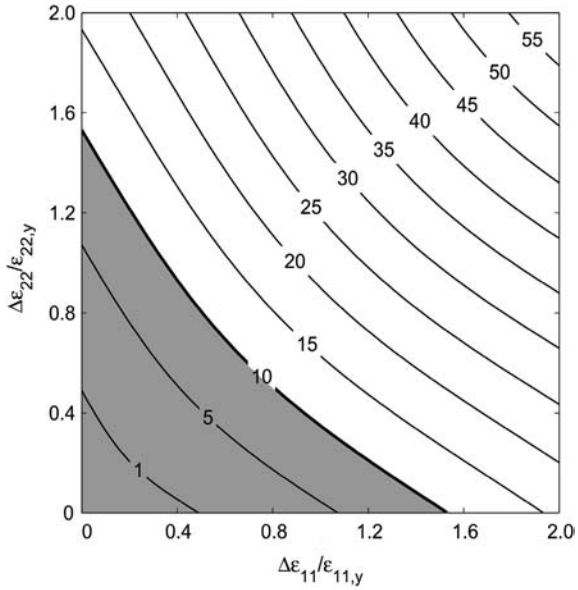

Figure 28.
Iso-error map corresponding to biaxial state on the yield surface for the forward Euler method

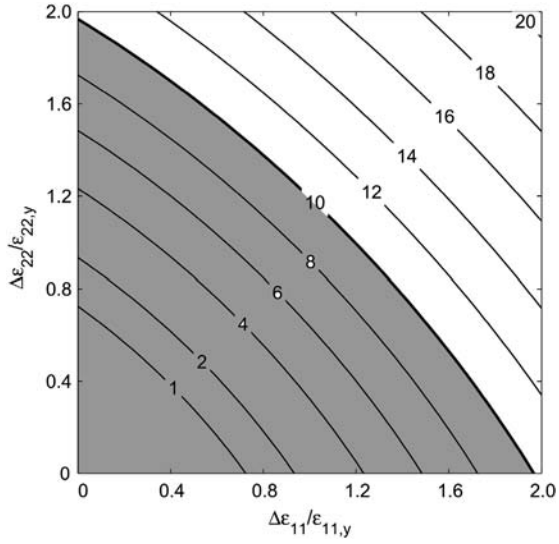

Figure 29.
Iso-error map corresponding to biaxial state on the yield surface for the present work

Euler approach, the numerical integration algorithm and its consistent tangent operator are presented. This kind of formulation for the nonlinear mixed hardening is not available in the literature.

In this investigation, a broad set of numerical tests is performed. The piecewise loading histories with different load steps are considered. These studies confirm

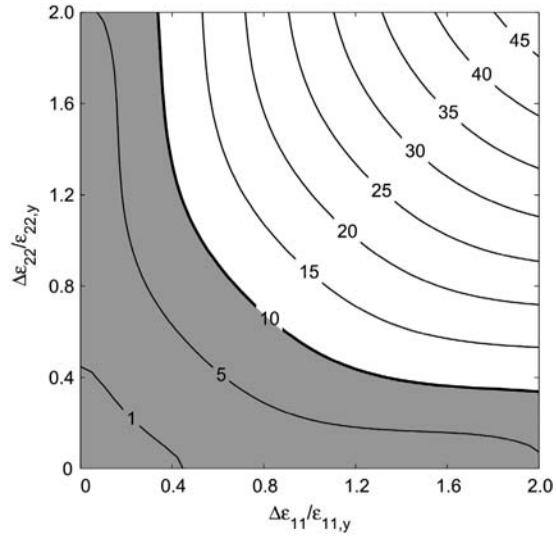

Figure 30.
Iso-error map corresponding to pure shear state on the yield surface for the forward Euler method

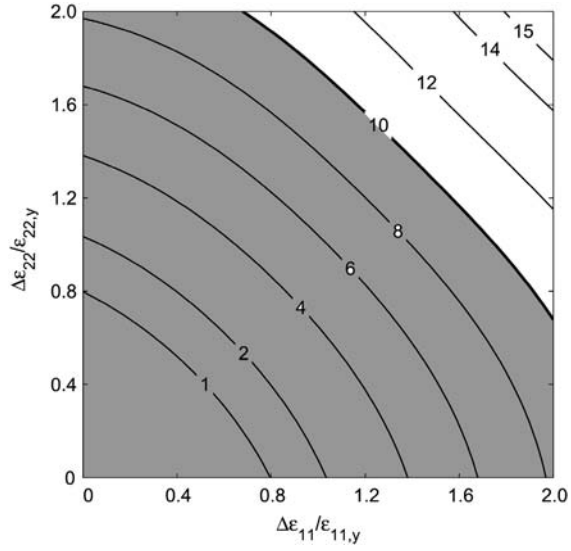

Figure 31.
Iso-error map corresponding to pure shear state on the yield surface for the present work

the robustness and high efficiency of the suggested formulation. To clarify the accuracy, the iso-error maps are provided for both the new exponential algorithm and forward Euler technique. The findings of the paper demonstrate that the proposed scheme gives very accurate results, even with large load steps.

References

Abdel-Karim, M. (2009), "Modified kinematic hardening rules for simulations of ratcheting", *Int. J. Plasticity*, Vol. 25, pp. 1560-87.

Abdel-Karim, M. and Ohno, N. (2000), "Kinematic hardening model suitable for ratcheting with steady-state", *Int. J. Plasticity*, Vol. 16, pp. 225-40.

Armstrong, P.J. and Frederick, C.O. (1966), "A mathematical representation of the multiaxial Bauschinger effect", Report RD/B/N731, CEGB, Central Electricity Generating Board, Berkeley.

Artioli, E., Auricchio, F. and Beirão da Veiga, L. (2006), "A novel 'optimal' exponential-based integration algorithm for von-Mises plasticity with linear hardening: theoretical analysis on yield consistency, accuracy, convergence and numerical investigations", *Int. J. Numer. Meth. Eng.*, Vol. 67 No. 4, pp. 449-98.

Artioli, E., Auricchio, F. and Beirão da Veiga, L. (2007), "Second-order accurate integration algorithms for von-Mises plasticity with a nonlinear kinematic hardening mechanism", *Comput. Meth. Appl. Mech. Eng.*, Vol. 196, pp. 1827-46.

Auricchio, F. and Beirão da Veiga, L. (2003), "On a new integration scheme for von-Mises plasticity with linear hardening", *Int. J. Numer. Meth. Eng.*, Vol. 56, pp. 1375-96.

Bari, S. and Hassan, T. (2000), "Anatomy of coupled constitutive models for ratcheting simulation", *Int. J. Plasticity*, Vol. 16, pp. 381-409.

Chaboche, J.L. (1986), "Time-independent constitutive theories for cyclic plasticity", *Int. J. Plasticity*, Vol. 2, pp. 149-88.

Chaboche, J.L. (1991), "On some modifications of kinematic hardening to improve the description of ratcheting effects", *Int. J. Plasticity*, Vol. 7, pp. 661-78.

Chaboche, J.L. (2008), "A review of some plasticity and viscoplasticity constitutive theories", *Int. J. Plasticity*, Vol. 24, pp. 1642-93.

Chakrabarty, J. (2006), *Theory of Plasticity*, 3rd ed., Elsevier Butterworth-Heinemann, Oxford.

Dafalias, Y.F. and Popov, E.P. (1976), "Plastic internal variables formalism of cyclic plasticity", *J. Appl. Mech.*, Vol. 43, pp. 645-50.

Hong, H.-K. and Liu, C.-S. (1999), "Internal symmetry in bilinear elastoplasticity", *Int. J. Non-Linear Mech.*, Vol. 34, pp. 279-88.

Hong, H.-K. and Liu, C.-S. (2000a), "Internal symmetry in the constitutive model of perfect elastoplasticity", *Int. J. Non-Linear Mech.*, Vol. 35, pp. 447-66.

Hong, H.-K. and Liu, C.-S. (2000b), "Lorentz group on Minkowski spacetime for construction of the two basic principles of plasticity", *Int. J. Non-Linear Mech.*, Vol. 36, pp. 679-86.

Hu, W., Wang, C.H. and Barter, S. (1999), "Analysis of cyclic mean stress relaxation and strain ratchetting behaviour of aluminium 7050", DSTO-RR-0153, DSTO Aeronautical and Maritime Research Laboratory, Melbourne.

Kan, Q.H., Kang, G.Z. and Zhang, J. (2007), "A unified visco-plastic constitutive model for uniaxial time-dependent ratchetting and its finite element implementation", *Theoretical and Applied Fracture Mechanics*, Vol. 47, pp. 133-44.

Kang, G.Z. (2004), "A visco-plastic constitutive model for ratcheting of cyclically stable materials and its finite element implementation", *Mech. Materials*, Vol. 36, pp. 299-312.

Kang, G.Z. (2006), "Finite element implementation of viscoplastic constitutive model with strain-range-dependent cyclic hardening", *Communication in Numerical Methods in Engineering*, Vol. 22, pp. 137-53.

Kang, G.Z., Ohno, N. and Nebu, A. (2003), "Constitutive modeling of strain range dependent cyclic hardening", *Int. J. Plasticity*, Vol. 19, pp. 1801-19.

Kobayashi, M. and Ohno, N. (2002), "Implementation of cyclic plasticity models based on a general form of kinematic hardening", *Int. J. Numer. Meth. Eng.*, Vol. 53, pp. 2217-38.

Kobayashi, M., Mukai, M., Takahashi, H., Ohno, N., Kawakami, T. and Ishikawa, T. (2003), "Implicit integration and consistent tangent modulus of a time-dependent non-unified constitutive model", *Int. J. Numer. Meth. Eng.*, Vol. 58, pp. 1523-43.

Kreig, R.D. and Kreig, D.B. (1977), "Accuracies of numerical solution methods for the elastic-perfectly plastic model", *J. Press. Vess. Technol. Trans. ASME*, Vol. 99, pp. 510-15.

Liu, C.-S. (2003), "Symmetry groups and the pseudo-Riemann spacetimes for mixed-hardening elastoplasticity", *Int. J. Solids Struct.*, Vol. 40, pp. 251-69.

Liu, C.-S. (2004), "Internal symmetry groups for the Drucker-Prager material model of plasticity and numerical integrating methods", *Int. J. Solids Struct.*, Vol. 41, pp. 3771-91.

Mroz, Z. (1967), "On the description of anisotropic work hardening", *J. Mech. Phys. Solids*, Vol. 15, pp. 163-75.

Ohno, N. (1982), "A constitutive model of cyclic plasticity with a nonhardening strain region", *J. Appl. Mech. ASME*, Vol. 49, pp. 721-7.

Ohno, N. and Kachi, Y. (1986), "A constitutive model of cyclic plasticity for nonlinear hardening materials", *J. Appl. Mech. ASME*, Vol. 53, pp. 395-403.

Ohno, N. and Wang, J.D. (1993), "Kinematic hardening rules with critical state of dynamic recovery, part I: formulations and basic features for ratcheting behavior", *Int. J. Plasticity*, Vol. 9, pp. 375-90.

Ortiz, M. and Popov, E.P. (1985), "Accuracy and stability of integration algorithms for elastoplastic constitutive relations", *Int. J. Numer. Meth. Eng.*, Vol. 21, pp. 1561-76.

Ortiz, M. and Simo, J.C. (1986), "An analysis of a new class of integration algorithms for elastoplastic constitutive relations", *Int. J. Numer. Meth. Eng.*, Vol. 23, pp. 353-66.

Prager, W. (1956), "A new method of analyzing stresses and strains in work hardening plastic solids", *J. Appl. Mech. ASME*, Vol. 23, pp. 493-6.

Rezaiee-Pajand, M. and Nasirai, C. (2007), "Accurate integration scheme for von-Mises plasticity with mixed-hardening based on exponential maps", *Engineering Computations*, Vol. 24 No. 6, pp. 608-35.

Rezaiee-Pajand, M. and Nasirai, C. (2008), "On the integration schemes for Drucker-Prager's elastoplastic models based on exponential maps", *Int. J. Numer. Meth. Eng.*, Vol. 74, pp. 799-826.

Rezaiee-Pajand, M. and Sinaie, S. (2009), "On the calibration of the Chaboche hardening model and a modified hardening rule for uniaxial ratcheting prediction", *Int. J. Solids Struct.*, Vol. 46, pp. 3009-17.

Rezaiee-Pajand, M., Nasirai, C. and Sharifian, M. (2010), "Application of exponential-based methods in integrating the constitutive equations with multicomponent kinematic hardening", *J. Eng. Mech. ASCE*, Vol. 136 No. 12, pp. 1502-18.

Rezaiee-Pajand, M., Sharifian, M. and Sharifian, M. (2011), "Accurate and approximate integrations of Drucker-Prager plasticity with linear isotropic and kinematic hardening", *European Journal of Mechanics A/Solids*, Vol. 30, pp. 345-61.

Rice, J.R. and Tracey, D.M. (1973), "Computational fracture mechanics", *Proceedings of the Symposium on Numerical Methods in Structural Mechanics, University of Illinois, Urbana, IL, USA*, p. 585.

Simo, J.C. and Hughes, T.J.R. (1998), *Computational Inelasticity*, Springer, New York, NY.

Tseng, N.T. and Lee, G.C. (1983), "Simple plasticity model of the two-surface type", *J. Eng. Mech. ASCE*, Vol. 109, pp. 795-810.

Wilkins, M.L. (1964), "Calculation of elastic-plastic flow", *Method of Computational Physics*, Vol. 3.

Zhang, Z., Delagnes, D. and Bernhart, G. (2002), "Anisothermal cyclic plasticity modeling of martensitic steels", *Int. J. Fatig.*, Vol. 24, pp. 635-48.

Appendix 1. Derivatives of the parameter A_i^c for different kinematic hardening models

For Chaboche models, which are presented in equations (14) and (15):

$$\frac{\partial A_i^c}{\partial \mathbf{e}_{n+1}} = 0 \tag{A1}$$

For Ohno-Wang model-1, which is given in equation (16):

$$\frac{\partial A_i^c}{\partial \mathbf{e}_{n+1}} = H_{nl,i}\mathrm{H}\left\{(\mathbf{n}^c)^{\mathrm{T}}\frac{\boldsymbol{\alpha}_{n,i}}{\|\boldsymbol{\alpha}_{n,i}\|}\right\}\mathrm{H}\left\{\boldsymbol{\alpha}_{n,i}^{\mathrm{T}}\boldsymbol{\alpha}_{n,i} - \frac{3}{2}\left(\frac{H_{\mathrm{kin},i}}{H_{nl,i}}\right)^2\right\}\frac{\partial \mathbf{n}^c}{\partial \mathbf{e}_{n+1}}\frac{\boldsymbol{\alpha}_{n,i}}{\|\boldsymbol{\alpha}_{n,i}\|} \tag{A2}$$

For Ohno-Wang model-2, which is presented in equation (17):

$$\frac{\partial A_i^c}{\partial \mathbf{e}_{n+1}} = H_{nl,i}\mathrm{H}\left\{(\mathbf{n}^c)^{\mathrm{T}}\frac{\boldsymbol{\alpha}_{n,i}}{\|\boldsymbol{\alpha}_{n,i}\|}\right\}\left(\frac{H_{nl,i}}{H_{\mathrm{kin},i}}\|\boldsymbol{\alpha}_{n,i}\|\right)^{q_i}\frac{\partial \mathbf{n}^c}{\partial \mathbf{e}_{n+1}}\frac{\boldsymbol{\alpha}_{n,i}}{\|\boldsymbol{\alpha}_{n,i}\|} \tag{A3}$$

For Abdel Karim-Ohno model, which is given equation (18):

$$\frac{\partial A_i^c}{\partial \mathbf{e}_{n+1}} = H_{nl,i}\mathrm{H}\left\{(\mathbf{n}^c)^{\mathrm{T}}\frac{\boldsymbol{\alpha}_{n,i}}{\|\boldsymbol{\alpha}_{n,i}\|} - \mu_i\right\}\mathrm{H}\left\{\boldsymbol{\alpha}_{n,i}^{\mathrm{T}}\boldsymbol{\alpha}_{n,i} - \frac{3}{2}\left(\frac{H_{\mathrm{kin},i}}{H_{nl,i}}\right)^2\right\}\frac{\partial \mathbf{n}^c}{\partial \mathbf{e}_{n+1}}\frac{\boldsymbol{\alpha}_{n,i}}{\|\boldsymbol{\alpha}_{n,i}\|} \tag{A4}$$

Appendix 2. Derivatives, which are appeared in the discrete consistent tangent matrix, for the forward Euler method

$$\frac{\partial \boldsymbol{\Sigma}'_{n+1}}{\partial \mathbf{e}_{n+1}} = \frac{\partial \mathbf{s}'_{n+1}}{\partial \mathbf{e}_{n+1}} - \frac{\partial \boldsymbol{\alpha}_{n+1}}{\partial \mathbf{e}_{n+1}} \tag{A5}$$

$$\frac{\partial \mathbf{s}'_{n+1}}{\partial \mathbf{e}_{n+1}} = 2G\left(\mathbb{I} - \frac{\partial \Delta \mathbf{e}^{\mathrm{p}}}{\partial \mathbf{e}_{n+1}}\right) \tag{A6}$$

$$\frac{\partial \Delta \mathbf{e}^{\mathrm{p}}}{\partial \mathbf{e}_{n+1}} = \frac{\partial \lambda}{\partial \mathbf{e}_{n+1}}(\mathbf{n}^c)^{\mathrm{T}} + \lambda\frac{\partial \mathbf{n}^c}{\partial \mathbf{e}_{n+1}} \tag{A7}$$

$$\frac{\partial \lambda}{\partial \mathbf{e}_{n+1}} = -2wG(\mathbf{n}^{\mathrm{c}})^{\mathrm{T}}\Delta\mathbf{e}\frac{\mathrm{d}\alpha}{\mathrm{d}\mathbf{e}_{n+1}} + 2wG(1-\alpha)\frac{\partial \mathbf{n}^{\mathrm{c}}}{\partial \mathbf{e}_{n+1}}\Delta\mathbf{e} + 2wG(1-\alpha)\mathbf{n}^{\mathrm{c}} + 2w^2G(1-\alpha)(\mathbf{n}^{\mathrm{c}})^{\mathrm{T}}\Delta\mathbf{e}\left(\frac{\partial \mathbf{n}^{\mathrm{c}}}{\partial \mathbf{e}_{n+1}}\sum_{i=1}^{m}A_i^{\mathrm{c}}\boldsymbol{\alpha}_{n,i}\right) + 2w^2G(1-\alpha)(\mathbf{n}^{\mathrm{c}})^{\mathrm{T}}\Delta\mathbf{e}\left\{\left[\sum_{i=1}^{m}\boldsymbol{\alpha}_{n,i}\left(\frac{\partial A_i^{\mathrm{c}}}{\partial \mathbf{e}_{n+1}}\right)^{\mathrm{T}}\right]\mathbf{n}^{\mathrm{c}}\right\} \tag{A8}$$

$$w = \frac{1}{2\bar{G} + \bar{b}(R_{\mathrm{s}} + R_0 - R_n) - (\mathbf{n}^{\mathrm{c}})^{\mathrm{T}}\sum_{i=1}^{m}A_i^{\mathrm{c}}\boldsymbol{\alpha}_{n,i}}$$

$$\frac{\partial \mathbf{n}^{\mathrm{c}}}{\partial \mathbf{e}_{n+1}} = \frac{1}{\|\Sigma^{\mathrm{c}}\|}\frac{\partial \Sigma^{\mathrm{c}}}{\partial \mathbf{e}_{n+1}} - \Sigma_{n+1}^{\mathrm{c}}\left(\frac{\partial \Sigma^{\mathrm{c}}}{\partial \mathbf{e}_{n+1}}\ \frac{\Sigma^{\mathrm{c}}}{\|\Sigma^{\mathrm{c}}\|^3}\right)^{\mathrm{T}} \tag{A9}$$

$$\frac{\partial \Sigma^{\mathrm{c}}}{\partial \mathbf{e}_{n+1}} = 2G\frac{\mathrm{d}\alpha}{\mathrm{d}\mathbf{e}_{n+1}}\Delta\mathbf{e}^{\mathrm{T}} + 2G\alpha\mathbb{I} \tag{A10}$$

$$\frac{\mathrm{d}\alpha}{\mathrm{d}\mathbf{e}_{n+1}} = T_1\frac{\mathrm{d}C}{\mathrm{d}\mathbf{e}_{n+1}} + T_2\frac{\mathrm{d}D}{\mathrm{d}\mathbf{e}_{n+1}} \tag{A11}$$

$$T_1 = \frac{1}{D}\left(\frac{C}{\sqrt{C^2 - DM}} - 1\right), \quad T_2 = -\frac{1}{D^2}\left(\frac{DM}{2\sqrt{C^2 - DM}} + \sqrt{C^2 - DM} - C\right) \tag{A12}$$

$$\frac{\mathrm{d}C}{\mathrm{d}\mathbf{e}_{n+1}} = 2G(\mathbf{s}_n - \boldsymbol{\alpha}_n), \quad \frac{\mathrm{d}D}{\mathrm{d}\mathbf{e}_{n+1}} = 2(2G)^2\Delta\mathbf{e} \tag{A13}$$

$$\frac{\partial a_{\mathrm{f}}}{\partial \mathbf{e}_{n+1}} = \left[\left(\mathbf{n}_{n+1}^{\mathrm{T}}\Sigma'_{n+1}\right)^2 - \|\Sigma'_{n+1}\|^2 + R_{n+1}^2\right]^{-(1/2)}\left[\left(\frac{\partial \mathbf{n}_{n+1}}{\partial \mathbf{e}_{n+1}}\Sigma'_{n+1} + \frac{\partial \Sigma'_{n+1}}{\partial \mathbf{e}_{n+1}}\mathbf{n}_{n+1}\right)\left(\mathbf{n}_{n+1}^{\mathrm{T}}\Sigma'_{n+1}\right) - \|\Sigma'_{n+1}\|\frac{\partial \|\Sigma'_{n+1}\|}{\partial \mathbf{e}_{n+1}} + R_{n+1}\frac{\partial R_{n+1}}{\partial \mathbf{e}_{n+1}}\right] - \frac{\partial \mathbf{n}_{n+1}}{\partial \mathbf{e}_{n+1}}\Sigma'_{n+1} - \frac{\partial \Sigma'_{n+1}}{\partial \mathbf{e}_{n+1}}\mathbf{n}_{n+1} \tag{A14}$$

$$\frac{\partial R_{n+1}}{\partial \mathbf{e}_{n+1}} = R_{\mathrm{s}}\bar{b}\ \exp(-\bar{b}\gamma_{n+1})\frac{\partial \lambda}{\partial \mathbf{e}_{n+1}} \tag{A15}$$

Appendix 3. Derivatives, which are appeared in the discrete consistent tangent matrix, for the exponential-based method

To calculate $\left(\partial \mathbf{X}_{n+1}^{\mathrm{s}}/\partial \mathbf{e}_{n+1}\right)$ and $\left(\partial X_{n+1}^{0}/\partial \mathbf{e}_{n+1}\right)$, which are appeared in equation (91), the expressions for $\mathbf{X}_{n+1}^{\mathrm{s}}$ and X_{n+1}^{0} are required. Utilizing equation (58) and assuming an elastic-plastic load step, the following equation can be obtained:

$$\mathbf{X}_{n+1} = \mathbb{G}^{\mathrm{p}}\mathbb{G}^{\mathrm{e}}\mathbf{X}_n = \mathbb{G}^{\mathrm{p}}\mathbf{X}^{\mathrm{c}} \tag{A16}$$

$$\mathbf{X}_{n+1}^{\mathrm{s}} = \mathbf{X}_n^{\mathrm{s}} + (a-1)\left(\Delta\hat{\boldsymbol{\Phi}}^{\mathrm{T}}\mathbf{X}_n^{\mathrm{s}}\right)\Delta\hat{\boldsymbol{\Phi}} + \alpha\frac{2G}{R_n}X_n^0\Delta\mathbf{e} + (a-1)\alpha\frac{2G}{R_n}X_n^0\left(\Delta\hat{\boldsymbol{\Phi}}^{\mathrm{T}}\Delta\mathbf{e}\right)\Delta\hat{\boldsymbol{\Phi}} + bX_n^0\Delta\hat{\boldsymbol{\Phi}} \tag{A17}$$

$$X_{n+1}^0 = b\left(\Delta\hat{\boldsymbol{\Phi}}^{\mathrm{T}}\mathbf{X}_n^{\mathrm{s}}\right) + b\alpha\frac{2G}{R_n}X_n^0(\Delta\hat{\boldsymbol{\Phi}}^{\mathrm{T}}\Delta\mathbf{e}) + aX_n^0 \tag{A18}$$

Now, taking the derivatives of $\mathbf{X}^{\mathrm{s}}_{n+1}$ and X^{0}_{n+1} with respect to $\mathbf{e}_{n+1}$, the following equations will be achieved:

$$\frac{\partial \mathbf{X}^{\mathrm{s}}_{n+1}}{\partial \mathbf{e}_{n+1}} = C_1\left[\Delta\hat{\mathbf{\Phi}}\left(\frac{\partial a}{\partial \mathbf{e}_{n+1}}\right)^{\mathrm{T}}\right] + C_2\left[\Delta\hat{\mathbf{\Phi}}\left(\frac{\partial \Delta\hat{\mathbf{\Phi}}}{\partial \mathbf{e}_{n+1}}\mathbf{X}^{\mathrm{s}}_{n}\right)^{\mathrm{T}}\right] + C_3\left(\frac{\partial \Delta\hat{\mathbf{\Phi}}}{\partial \mathbf{e}_{n+1}}\right) + C_4\left[\Delta\mathbf{e}\left(\frac{\mathrm{d}\alpha}{\mathrm{d}\mathbf{e}_{n+1}}\right)^{\mathrm{T}}\right] + C_5\left[\Delta\hat{\mathbf{\Phi}}\left(\frac{\mathrm{d}\alpha}{\mathrm{d}\mathbf{e}_{n+1}}\right)^{\mathrm{T}}\right] + C_6\left[\Delta\hat{\mathbf{\Phi}}\left(\frac{\partial \Delta\hat{\mathbf{\Phi}}}{\partial \mathbf{e}_{n+1}}\Delta\mathbf{e}\right)^{\mathrm{T}} + \Delta\hat{\mathbf{\Phi}}\Delta\hat{\mathbf{\Phi}}^{\mathrm{T}}\right] + C_7\left[\Delta\hat{\mathbf{\Phi}}\left(\frac{\partial b}{\partial \mathbf{e}_{n+1}}\right)^{\mathrm{T}}\right] + C_8\mathbb{I} \tag{A19}$$

$$\begin{aligned} C_1 &= \Delta\hat{\mathbf{\Phi}}^{\mathrm{T}}\mathbf{X}^{\mathrm{s}}_{n} + \alpha\frac{2G}{R_n}X^{0}_{n}(\Delta\hat{\Phi}^{\mathrm{T}}\Delta\mathbf{e}), \quad C_2 = a-1 \\ C_3 &= (a-1)\left(\Delta\hat{\mathbf{\Phi}}^{\mathrm{T}}\mathbf{X}^{\mathrm{s}}_{n}\right) + (a-1)\alpha\frac{2G}{R_n}X^{0}_{n}(\Delta\hat{\mathbf{\Phi}}^{\mathrm{T}}\Delta\mathbf{e}) + bX^{0}_{n} \\ C_4 &= \frac{2G}{R_n}X^{0}_{n}, \\ C_5 &= (a-1)\alpha\frac{2G}{R_n}X^{0}_{n}(\Delta\hat{\mathbf{\Phi}}^{\mathrm{T}}\Delta\mathbf{e}) \\ C_6 &= (a-1)\alpha\frac{2G}{R_n}X^{0}_{n}, \quad C_7 = X^{0}_{n}, \quad C_8 = \alpha\frac{2G}{R_n}X^{0}_{n} \end{aligned} \tag{A20}$$

$$\frac{\partial X^{0}_{n+1}}{\partial \mathbf{e}_{n+1}} = D_1\frac{\partial b}{\partial \mathbf{e}_{n+1}} + D_2\left(\frac{\partial \Delta\hat{\mathbf{\Phi}}}{\partial \mathbf{e}_{n+1}}\mathbf{X}^{\mathrm{s}}_{n}\right) + D_3\frac{\mathrm{d}\alpha}{\mathrm{d}\mathbf{e}_{n+1}} + D_4\left(\frac{\partial \Delta\hat{\mathbf{\Phi}}}{\partial \mathbf{e}_{n+1}}\Delta\mathbf{e} + \Delta\hat{\mathbf{\Phi}}\right) + D_5\frac{\partial a}{\partial \mathbf{e}_{n+1}} \tag{A21}$$

$$\begin{aligned} &D_1 = \Delta\hat{\mathbf{\Phi}}^{\mathrm{T}}\mathbf{X}^{\mathrm{s}}_{n} + \alpha\frac{2G}{R_n}X^{0}_{n}(\Delta\hat{\mathbf{\Phi}}^{\mathrm{T}}\Delta\mathbf{e}), \quad D_2 = b, \quad D_3 = b\frac{2G}{R_n}X^{0}_{n}(\Delta\hat{\mathbf{\Phi}}^{\mathrm{T}}\Delta\mathbf{e}) \\ &D_4 = b\alpha\frac{2G}{R_n}X^{0}_{n}, \quad D_5 = X^{0}_{n} \end{aligned} \tag{A22}$$

$$\frac{\mathrm{d}\alpha}{\mathrm{d}\mathbf{e}_{n+1}} = T_1\frac{\mathrm{d}C}{\mathrm{d}\mathbf{e}_{n+1}} + T_2\frac{\mathrm{d}D}{\mathrm{d}\mathbf{e}_{n+1}} \tag{A23}$$

$$T_1 = \frac{1}{D}\left(\frac{C}{\sqrt{C^2 - DM}} - 1\right), \quad T_2 = -\frac{1}{D^2}\left(\frac{DM}{2\sqrt{C^2 - DM}} + \sqrt{C^2 - DM} - C\right) \tag{A24}$$

$$\frac{\mathrm{d}C}{\mathrm{d}\mathbf{e}_{n+1}} = \frac{2G}{R_n}X^{0}_{n}\mathbf{X}^{\mathrm{s}}_{n}, \quad \frac{\mathrm{d}D}{\mathrm{d}\mathbf{e}_{n+1}} = 2\left(\frac{2G}{R_n}X^{0}_{n}\right)^{2}\Delta\mathbf{e} \tag{A25}$$

$$\frac{\partial \Delta\hat{\mathbf{\Phi}}}{\partial \mathbf{e}_{n+1}} = \frac{1}{\|\Delta\mathbf{\Phi}\|}\frac{\partial \Delta\mathbf{\Phi}}{\partial \mathbf{e}_{n+1}} - \frac{1}{\|\Delta\mathbf{\Phi}\|}\left[\Delta\hat{\mathbf{\Phi}}\left(\frac{\partial \Delta\mathbf{\Phi}}{\partial \mathbf{e}_{n+1}}\Delta\hat{\Phi}\right)^{\mathrm{T}}\right] \tag{A26}$$

$$\frac{\partial \Delta \boldsymbol{\Phi}}{\partial \mathbf{e}_{n+1}} = \mathbb{I} + w\left(\sum_{i=1}^{m} A_i^{\mathrm{c}} \boldsymbol{\alpha}_{n,i}\right)(\mathbf{n}^{\mathrm{c}})^{\mathrm{T}} + w\left[\left(\sum_{i=1}^{m} A_i^{\mathrm{c}} \boldsymbol{\alpha}_{n,i}\right)\Delta \mathbf{e}^{\mathrm{T}}\right]\frac{\partial \mathbf{n}^{\mathrm{c}}}{\partial \mathbf{e}_{n+1}}$$
$$+ w(\mathbf{n}^{\mathrm{c}})^{\mathrm{T}}\Delta \mathbf{e}\sum_{i=1}^{m} \boldsymbol{\alpha}_{n,i}\left(\frac{\partial A_i^{\mathrm{c}}}{\partial \mathbf{e}_{n+1}}\right)^{\mathrm{T}} + w^2(\mathbf{n}^{\mathrm{c}})^{\mathrm{T}}\Delta \mathbf{e}\left(\sum_{i=1}^{m} A_i^{\mathrm{c}} \boldsymbol{\alpha}_{n,i}\right)$$
$$\times\left(\frac{\partial \mathbf{n}^{\mathrm{c}}}{\partial \mathbf{e}_{n+1}}\sum_{i=1}^{m} A_i^{\mathrm{c}} \boldsymbol{\alpha}_{n,i}\right)^{\mathrm{T}} + w^2(\mathbf{n}^{\mathrm{c}})^{\mathrm{T}}\Delta \mathbf{e}\left(\sum_{i=1}^{m} A_i^{\mathrm{c}} \boldsymbol{\alpha}_{n,i}\right) \tag{A27}$$
$$\times\left\{\left[\sum_{i=1}^{m} \boldsymbol{\alpha}_{n,i}\left(\frac{\partial A_i^{\mathrm{c}}}{\partial \mathbf{e}_{n+1}}\right)^{\mathrm{T}}\right]\mathbf{n}^{\mathrm{c}}\right\}^{\mathrm{T}}$$

$$w = \frac{1}{2\bar{G} + \bar{b}(R_{\mathrm{s}} + R_0 - R_n) - (\mathbf{n}^{\mathrm{c}})^{\mathrm{T}}\sum_{i=1}^{m} A_i^{\mathrm{c}} \boldsymbol{\alpha}_{n,i}}$$

$$\frac{\partial \mathbf{n}^{\mathrm{c}}}{\partial \mathbf{e}_{n+1}} = \alpha\frac{2G}{R_n}\mathbb{I} + \frac{2G}{R_n}\left[\Delta \mathbf{e}\left(\frac{\mathrm{d}\alpha}{\mathrm{d}\mathbf{e}_{n+1}}\right)^{\mathrm{T}}\right] \tag{A28}$$

$$\frac{\partial a}{\partial \mathbf{e}_{n+1}} = b\frac{2G}{R_n}\left[(1-\alpha)\frac{\partial \Delta \boldsymbol{\Phi}}{\partial \mathbf{e}_{n+1}}\Delta \hat{\boldsymbol{\Phi}} - \|\Delta \boldsymbol{\Phi}\|\frac{\mathrm{d}\alpha}{\mathrm{d}\mathbf{e}_{n+1}}\right] \tag{A29}$$

$$\frac{\partial b}{\partial \mathbf{e}_{n+1}} = a\frac{2G}{R_n}\left[(1-\alpha)\frac{\partial \Delta \boldsymbol{\Phi}}{\partial \mathbf{e}_{n+1}}\Delta \hat{\boldsymbol{\Phi}} - \|\Delta \boldsymbol{\Phi}\|\frac{\mathrm{d}\alpha}{\mathrm{d}\mathbf{e}_{n+1}}\right] \tag{A30}$$

Moreover, the term $(\partial R_{n+1}/\partial \mathbf{e}_{n+1})$, which is appeared in equation (91), will be obtained by taking the derivative of equation (71) with respect to $\mathbf{e}_{n+1}$, as follows:

$$\frac{\partial R_{n+1}}{\partial \mathbf{e}_{n+1}} = \bar{b}R_{\mathrm{s}}\ \exp(-\bar{b}\gamma_{n+1})\frac{\partial \gamma_{n+1}}{\partial \mathbf{e}_{n+1}} \tag{A31}$$

The derivative $(\partial \gamma_{n+1}/\partial \mathbf{e}_{n+1})$ in the last equation can be calculated by using equation (45). For the case $\bar{b} = 0$, the result is as follows:

$$\frac{\partial \gamma_{n+1}}{\partial \mathbf{e}_{n+1}} = \frac{1}{X_{n+1}^0}\ \frac{R_0}{2\bar{G}}\ \frac{\partial X_{n+1}^0}{\partial \mathbf{e}_{n+1}} \tag{A32}$$

Also, for the case $\bar{b} \neq 0$, the derivative may be obtained by the following equation:

$$\frac{\partial \gamma_{n+1}}{\partial \mathbf{e}_{n+1}} = \frac{\beta R_0\ \exp(\bar{b}\gamma_{n+1})}{\bar{b}\left[(1-\beta)(R_0 + R_s)\ \exp(\bar{b}\gamma_{n+1}) + \beta R_s\right]}$$
$$\times\left(\frac{(R_0 + R_s)\ \exp(\bar{b}\gamma_{n+1}) - R_s}{R_0}\right)^{(\beta-1)/\beta}\frac{\partial X_{n+1}^0}{\partial \mathbf{e}_{n+1}} \tag{A33}$$

About the authors

Mohammad Rezaiee-Pajand received his PhD in Structural Engineering from University of Pittsburgh, Pittsburgh, PA, USA. He is currently a Professor at Ferdowsi University of Mashhad (FUM), Mashhad, Iran. His research interests are nonlinear analysis, finite element method, structural optimization and numerical techniques. Mohammad Rezaiee-Pajand is the corresponding author and can be contacted at: mrpajand@yahoo.com

Cyrus Nasirai received his PhD in Structural Engineering from Ferdowsi University of Mashhad (FUM), Mashhad, Iran. He is currently an Assistant Professor at Islamic Azad University – Mashhad branch. He has been involved in the design and construction of many civil engineering structures. His research interests are nonlinear finite element method, computational mechanics, earthquake engineering and structural dynamics.

Mehrzad Sharifian is a PhD student of Structural Engineering at Ferdowsi University of Mashhad (FUM), Mashhad, Iran. His research interests are nonlinear finite element method, computational mechanics of solids and structures and structural dynamics.